
Research Article: New Research | Neuronal Excitability

After-hyperpolarization promotes the firing of mitral cells through a voltage dependent modification of action potential threshold

<https://doi.org/10.1523/ENEURO.0401-21.2021>

Cite as: eNeuro 2022; 10.1523/ENEURO.0401-21.2021

Received: 27 September 2021

Revised: 22 November 2021

Accepted: 13 December 2021

This Early Release article has been peer-reviewed and accepted, but has not been through the composition and copyediting processes. The final version may differ slightly in style or formatting and will contain links to any extended data.

Alerts: Sign up at www.eneuro.org/alerts to receive customized email alerts when the fully formatted version of this article is published.

Copyright © 2022 Fourcaud-Trocmé et al.

This is an open-access article distributed under the terms of the Creative Commons Attribution 4.0 International license, which permits unrestricted use, distribution and reproduction in any medium provided that the original work is properly attributed.

Title:

After-hyperpolarization promotes the firing of mitral cells through a voltage dependent modification of action potential threshold

Abbreviated title: AHP promotes mitral cells' firing

Author names and affiliation:

Fourcaud-Trocmé Nicolas*, Zbili Mickaël*, Duchamp-Viret Patricia, Kuczewski Nicola

* Equal contribution

Centre de Recherche en Neurosciences de Lyon, CNRS UMR 5292 - INSERM U 1028 - Université Claude Bernard Lyon 1, Centre Hospitalier Le Vinatier - Bâtiment 462 – Neurocampus, 95 boulevard Pinel, 69675 Bron Cedex

Author contributions

NFT, PDV and NK designed the research, NK performed the experiments, NFT, MZ and NK analyzed data, NFT, MZ, PDV and NK wrote the paper.

Correspondence should be addressed to (include email address):

patrica.viret@cnrs.fr

nicola.kuczewski@univ-lyon1.fr

Number of figures: 10

Number of tables: 0

Number of multimedia: 0

Number of words for abstract: 233

Number of words for significance statement: 127

Number of words for introduction: 440

Number of words for discussion: 1638

Acknowledgment:

This work was supported by the CNRS, INSERM, and Lyon 1 University.
We are grateful to Marco Canepari for reading the manuscript and suggestions.

Conflict of interest

None of the authors has any conflict of interest

Funding

No funding was specifically allocated for this work

Additional information:

Data availability

51 All raw electrophysiological traces, script for trace analysis, data analysis and model scripts are available at
52 Open Science Framework (<https://osf.io/s2dbw/>)
53
54 Key words: AHP, olfactory bulb, burst firing, rat, patch-clamp, sodium channel

Abstract

In the olfactory bulb, mitral cells (MCs) display a spontaneous firing that is characterized by bursts of action potentials (APs) intermixed with silent periods. Intra-burst firing frequency and duration are heterogeneous among MCs and increase with membrane depolarization. By using patch clamp recording on rat slices, we dissected out the intrinsic properties responsible of this bursting activity. We showed that the threshold of AP generation dynamically changes as a function of the preceding trajectory of the membrane potential. In fact, the AP threshold became more negative when the membrane was hyperpolarized and had a recovering rate inversely proportional to the membrane repolarization rate. Such variations appeared to be produced by changes in the inactivation state of voltage dependent Na^+ channels. Thus, AP initiation was favored by hyperpolarizing events, such as negative membrane oscillations or inhibitory synaptic input. After the first AP, the following fast afterhyperpolarization (fast AHP) brought the threshold to more negative values and then promoted the emission of the following AP. This phenomenon was repeated for each AP of the burst making the fast AHP a regenerative mechanism that sustained the firing, AHP with larger amplitudes and faster repolarizations being associated with larger and higher frequency bursts. Burst termination was found to be due to the development of a slow repolarization component of the AHP (slow AHP). Overall, the AHP characteristics appeared as a major determinant of the bursting properties.

Significance statement

Mitral cells (MCs) in the olfactory bulb are the main relay of olfactory information towards higher cortical areas and their firing activity provides a substrate for olfactory information. The MC intrinsic dynamics generate a discharge of action potentials (APs) in burst patterns whose underlying mechanisms are not yet elucidated. Here, we show the importance of the AP after-hyperpolarization (AHP) in this process. The fast AHP component increases the availability of sodium channels which facilitates the generation of burst discharge. In addition, the late manifestation of the slow AHP component returns the availability of sodium channel to their initial state and leads to the termination of burst. Overall we demonstrate that burst properties of MCs are determined by AHP characteristics.

81

82

Introduction

83

84

85

86

87

88

89

90

91

92

93

94

95

96

97

98

99

00

01

02

03

04

05

06

07

08

The AHP that follows the action potential is generally seen as an inhibitory mechanism that limits neuronal activity, by promoting firing frequency adaptation and termination of AP burst (Schwindt et al., 1988; Faber & Sah, 2007; Adelman et al., 2012; Reuveni & Barkai, 2018). The main mechanism underlying AHP is the activation of voltage- and calcium-dependent potassium currents. However, in some neuronal types, such as MCs, main output neurons of the olfactory bulb, the synaptic transmission also contributes to the AHP shape (Duménieu et al., 2015). Differences in the activation-inactivation kinetics and calcium sensitivity of the different subtypes of potassium channels, underlying AHP, are responsible for a division of its course into three successive components, a fast (fAHP), a medium (mAHP) and a slow (sAHP), which differ in onset times, rise and decay kinetics (Schwindt et al., 1988; Sah & Faber, 2002; Andrade et al., 2012). The relative contribution of each component evolves during the neuronal discharge making the AHP shape dependent on the preceding neuronal activity (Duménieu et al., 2015). The inhibitory action of the AHP is generally attributed to the potassium channels which prevent excitatory currents to bring the membrane potential (V_m) to the AP threshold (Rubin & Cleland, 2006). This vision may however lead to neglect the possibility that AHP could potentially have a pro-excitatory effect through the deinactivation of some voltage dependent channels, such as calcium T-type and sodium ones (Deister et al., 2009; Cain & Snutch, 2010; Platkiewicz & Brette, 2011; Iyer et al., 2017). Such deinactivation would promote neuronal firing when the V_m moves back to the resting state value.

MCs present a spontaneous firing activity which is characterized by AP clusters (= bursts) interspaced by silent periods (Desmaisons et al., 1999). This activity is mainly due to intrinsic membrane properties, since it could be observed in pharmacologically isolated MCs, in olfactory bulb slices (Balu et al., 2004). The cellular mechanisms behind MC bursting activity remain to be elucidated. Balu and Strowbridge (2004) proposed that the burst termination was due to the build-up of the slow AHP during repetitive firing. A computational model refined this idea by proposing that burst termination is not due to the accumulation of classical AHP currents but rather by the progressive deinactivation of potassium IA current along the consecutive AHPs of the burst (Rubin & Cleland, 2006). However, the mechanisms that trigger the burst, maintain the sustained firing and determine the number of APs or their frequency remain largely unknown.

Here we provide evidence that, through a dynamic change of AP threshold, the modification of V_m

09 associated to the AHP act both as a burst regeneration process and as a burst termination mechanism. In this
10 way the AHP characteristics play a pivotal role in determining the firing properties of MCs.

12 **Methods**

13 **Animals**

14 Animal handling was conducted in accordance with the European Community Council Directive 86/609/EEC.
15 Experiments were performed in P30-P42 male Long Evans rats (Janvier, Le Genest-Saint-Isle, France). The
16 animals were maintained on normal light cycle and ad libitum accessed to water and food.

17 **Slice preparation.**

18 Animals were anaesthetized with an intra-peritoneal injection of ketamine (50 mg/ml) and then, decapitated.
19 The head was quickly immersed in ice-cold (2-4°C) carbogenized artificial cerebrospinal fluid (ACSF;
20 composition: 125 mM NaCl, 4 mM KCl, 25 mM NaHCO₃, 0.5 mM CaCl₂, 1.25 mM NaH₂PO₄, 7 mM MgCl₂
21 and 5.5 mM glucose; pH = 7.4) oxygenated with 95% O₂, 5% CO₂. The osmolarity was adjusted to 320 mOsm
22 with sucrose. The two olfactory bulbs were removed from the cranial cavity and cut in horizontal slices (400 μm
23 thick) using a Leica VT1000s vibratome (Leica Biosystems, France). Slices were then incubated in Gibb's
24 chamber at 30 ±1°C in modified calcium and magnesium ACSF (CaCl₂=2 mM and MgCl₂ = 1 mM).

27 **Electrophysiological recordings.**

28 Slices were transferred into a recording chamber mounted on an upright microscope (Axioskop FS, Zeiss) and
29 perfused with oxygenated ACSF (4 ml/min) at 30 ±1°C. Neurons were visualized using a 40X objective and a
30 Hamamatsu "Orca Flash 4.0" camera. Measurements were performed with a RK 400 amplifier (BioLogic,
31 France). Data were acquired with a sampling frequency of 25 kHz on a PC-Pentium D computer using a 12-bit
32 A/D-D/A converter (Digidata 1440A, Axon Instruments) and PClamp10 software (Axon Instruments). Patch-
33 clamp recordings were achieved with borosilicate pipettes (o.d.: 1.5 mm; i.d.: 1.17 mm; Clark Electromedical
34 Instruments), filled with the intracellular solution (131 mM K-gluconate, 10 mM HEPES, 1 mM EGTA, 1 mM
35 MgCl₂, 2 mM ATP-Na₂, 0.3 mM GTP-Na₃, and 10 mM phosphocreatine; pH = 7.3, 290 mOsm). In our
36 experimental conditions, the equilibrium potential of chloride ions (E_{Cl}) was -110 mV, and that of

37 potassium ions (E_k) was -92 mV. The calculated junction potential of 13 mV was corrected offline.

38 **Data analysis**

39 *Evoked activity (Figures 4,5 and 9):*

40 Experiments were performed in current clamp. A small steady membrane hyperpolarization was ensured by
41 negative current injection in order to prevent spontaneous firing. For the experiments investigating the
42 relationship between the level of hyperpolarization and the AP threshold, two successive APs were generated by
43 two 3 ms depolarizing current steps applied at 6 s interval; the second step being preceded by membrane
44 hyperpolarization varying in amplitude and duration. Some data were excluded from the analysis when the
45 average resting potential, in the 500 ms preceding the depolarizing step, differed by more than 2 mV between
46 the two evoked APs. In experiments investigating the relationship between the speed of repolarization-
47 hyperpolarization and AP threshold, current ramps of variable slopes were applied. The AP threshold was
48 calculated from the first AP generated during the ramp: it was defined as being the first point with a strict
49 positive acceleration (second derivative of its V_m) during the AP rising phase, before it reaches its maximum
50 depolarizing rate.

51 *Sodium currents measurements (Figure 5):*

52 Experiments were performed in voltage clamp in the presence of 0.3 mM cadmium, 4 mM Nickel 4, 10 mM
53 Tetraethylammonium (TEA), 10 mM 4-Aminopyridine (4AP), 10 mM 2,3-Dioxo-6-nitro-1,2,3,4-
54 tetrahydrobenzo[f]quinoxaline-7-sulfonamide disodium salt (NBQX), 5 mM 2-APV, D-APV, D-2-amino-5-
55 phosphonovalerate (D-APV) and 5 Mm Bicuculline.

56 *Spontaneous activity (Figures 2, 3, 6, 7 and 8):*

57 Spontaneous activity was recorded from cells at their resting membrane potential (17 cells with a resting
58 potential around -60 mV, and 15 cells around -55 mV). In some cells, we needed to inject a small steady
59 depolarizing current to bring the MP from around -60 mV to about -55 mV in order to generate spontaneous-like
60 activity (15 cells) while in 2 cells we needed to inject a small hyperpolarizing current to transform tonic firing to
61 burst firing. We did not observe any qualitative differences between all groups of cells in our analyses, they are
62 thus pooled in the result description.

63 APs were detected each time the membrane potential crossed -23 mV (detection potential) from below, and

64 the minimum interspike interval was set at 1 ms. In one cell, the detection potential was set at -43 mV because
65 of the low amplitude of first AP in bursts.

66 Bursts were detected based on a time-interval threshold, for the interspike intervals (tISI) below which, two
67 occurring APs were assigned to the same burst. To achieve this, tISI was first set at 90 ms for all analyzed MCs,
68 and then adapted cell by cell in a recursive manner through the following procedure: we computed a new tISI as
69 the median ISI of all detected bursts in a cell, plus 4 times their median absolute deviation (except for one cell:
70 only 0.8 times its median absolute deviation, cell label 8 in the figures). If the new tISI was lower than the
71 previous one, we used it to detect again bursts of the cell and restarted over a new tISI computation and so on,
72 until the new tISI was larger than the last one (final burst ISI thresholds: mean: 47 ms, SD: 19 ms, range 13-90
73 ms). The reliability of the burst detection method was assessed by visual inspection of traces. In our analyses,
74 we will always refer to the burst size as the number of APs within each burst.

75 In the following we describe how AP parameters or burst parameters used in this study were measured. An
76 example of Vm trace with a schematic of most of the measures of interest is shown in Figure 1.

77 Because some recorded MCs showed slow fluctuations of subthreshold Vm, the latter was computed before
78 each burst. If the interval without AP preceding a burst (interburst interval) lasted at least 200 ms, we defined
79 the burst resting potential (V_{rest}) as the median Vm during the interburst interval (excluding half of the tISI at
80 the beginning and 5 ms at the end). We also defined subthreshold fluctuation amplitude as the maximum Vm on
81 the same interval. If the interburst interval lasted less than 200 ms, V_{rest} and subthreshold fluctuation
82 amplitudes were defined as the same as for the preceding burst. In some figures (see legends), traces are aligned
83 on V_{rest} which was then set at 0 mV.

84 For each detected AP, we computed its voltage threshold (AP threshold) as the first point with a strictly positive
85 acceleration (second derivative of Vm) during the AP rising phase before Vm reaches its maximum positive
86 acceleration rate. In this study, we often used the relative AP threshold defined as the difference between AP
87 threshold and V_{rest} .

88 The pre-AP potential was the first negative Vm peak that preceded the AP threshold. It was detected by stepping
89 backward in time starting from AP threshold by 1 ms steps and, stopping as soon as a Vm rebound of at least 0.4
90 mV (relatively to the lowest Vm in the interval from current time step up to AP threshold time) was found.

91 The pre-AP potential was defined as the lowest V_m between the rebound time and the AP threshold time.

92 Pre-AP slope was the slope of the V_m course, preceding the first AP of the burst. When pre-AP potential
93 occurred more than 5 ms before the AP threshold time, the pre-AP slope was obtained by a linear regression of
94 the V_m course during the 5 ms before AP threshold. When pre-AP potential occurred less than 5 ms before AP
95 threshold, the pre-AP slope was obtained by a linear regression of V_m course in a range of 20% to 80% from the
96 pre-AP potential (0%) to the AP threshold (100%).

97 AHP amplitude was calculated by making the difference between the lowest V_m between two consecutive APs
98 (or in the 300 ms following the AP, if the ISI interval was too long) and V_{rest} . Note that according to our
99 convention AHP amplitudes are negative numbers.

00 The AHP slope was defined as the slope of a linear regression of V_m between the AHP peak and next AP
01 threshold, but restricted to a 20%-60% V_m range starting from AHP peak (0%) up to previous AP threshold
02 potential (100%). The V_m range for linear regression was indeed based on the preceding AP, in order to allow
03 computing the AHP slope following the last AP of a burst in the same way as the AHP slopes within the burst.

04 The AHP duration was defined as the period from AHP peak to next AP threshold time. The intra burst
05 frequency was defined as the average of the inverse ISIs within burst.

06 We noticed that following a burst, a slow AHP component induced a slow repolarization of the V_m toward
07 V_{rest} . To quantitatively characterize this component for each MC, we selected all bursts with a following
08 interburst interval of at least 500 ms. Electrophysiological traces were aligned on the AHP peak following the
09 last AP and a median trace was calculated. We then fitted this median trace from 50 ms to 500 ms after the AHP
10 peak with a single exponential which gave the slow AHP time constant. Because of our choice of a minimum
11 interval of 500 ms, some cells had no burst selected for median computation, the fit was thus possible in only 42
12 out of the 49 cells used in this study.

13 *Synaptically evoked activity:*

14 Experiments were performed in current clamp at MC resting membrane potential. Synaptic activity was
15 produced by 0.1 ms electrical stimulation (8-10 mA) of the olfactory nerve layer produced by a bipolar
16 electrode. Firing analysis was performed as for spontaneous activity.

17

18 Threshold linear model

19 In order to predict the expected AP threshold following the last burst AP, for each cell, we fitted a model of
20 intra-burst AP threshold as a linear combination of AHP amplitude, AHP slope, AHP duration and V_{rest} using
21 an Ordinary Least Square regression method. Note that we also tested models taking into account interactions
22 between these parameters but the increase in fit reliability (based on the Bayesian information criterion) was
23 negligible and did not justify taking these interactions into account.

24 Once a model was fitted for a given cell, we could predict the expected AP threshold following each burst last-
25 AP as a function of time elapsed after the last AHP maximum time (which gave the AHP duration parameter,
26 other model parameters being constant).

27

28 Burst size and burst frequency linear models

29 In order to quantify the dependence of burst size and burst frequency on fast and slow AHP parameters, we
30 pooled data from all cells and fitted models of burst size and burst frequency as a linear combination of V_{rest} ,
31 AHP amplitude and AHP slope (both measured during the first AHP within the burst) and their interactions.
32 Linear models were fitted using an Ordinary Least Square regression method. Two additional models including
33 the slow AHP time constant (measured once for each cell as stated above) were fitted and statistically compared
34 to the previous models with type I anovas. Only bursts of more than 3 APs were included in this analysis.
35 Normality and heteroscedasticity of residuals were checked visually, and required to transform the endogenous
36 variables before model fitting as follow: $\log(\log(\text{burst size}))$ and $\log(\text{burst frequency})$.

37

38 Neuron computational model

39 A single compartment model was simulated with NEURON 7.8. All simulations were run with 100- μ s time
40 steps. The nominal temperature was 30°C. The voltage dependence of activation and inactivation of Hodgkin-
41 Huxley-based conductance models were taken from (Hu et al., 2009) for N_{av} and K_{DR} and from (Rubin &
42 Cleland, 2006) for I_A . The equilibrium potentials for Na^+ , K^+ , and passive channels were set to +90, -91 and -
43 28.878 mV, respectively. We began by constructing a model with the following conductance's densities: 0.02
44 S/cm², 0.0002 S/cm², 0.003 S/cm² and 3.33×10^{-5} S/cm² for N_{av} , K_{DR} , I_A and passive channels, respectively.

45 This model presented a resting membrane potential of -60 mV without holding current injection. In all the other
46 model configurations, we injected a holding current during the simulation to maintain the resting membrane
47 potential at -60 mV.

48 In Figure 5, no I_A conductance was implemented in the model. The conductance density of Nav was set to 0.02
49 S/cm², 0.005 S/cm² or 0.0025 S/cm². The holding current was set to -0.826 pA, -29.49 pA and -29.26 pA
50 respectively. Spikes were induced by 3 ms positive current steps of 400 pA. Hyperpolarizations before APs
51 were induced by 50 ms negative current steps whose amplitudes were set in order to obtain a pre-AP membrane
52 potential from -60 mV to -70 mV. AP threshold was defined by the voltage point at which the first time
53 derivative (dV/dt) went above 40 mV/ms. The curve of AP threshold vs. pre-AP activatable Nav-conductance
54 was constructed by varying Nav-conductance density from 0.04 to 0.0025 S/cm², inducing one spike from
55 resting membrane potential and measuring AP threshold. The values of pre-AP activatable Nav-conductance
56 were obtained by multiplying the percentage of non-inactivated Nav-conductance - just before the positive
57 current step - by the total Nav- conductance density.

58 In Figure 9, the Nav-conductance density was set to 0.02 S/cm². The I_A conductance density was set to 0 or
59 0.003 S/cm². The I_A conductance was either directly taken from Rubin and Cleland (2006) or modified to get
60 biophysics closer to previously published I_A biophysics (Amendola et al., 2012). The modifications were done
61 on the inactivation of I_A conductance: modified I_A displayed a more depolarized half-inactivation (-90 mV
62 instead of -110 mV), a larger slope of inactivation curve (0.1 mV⁻¹ instead of 0.056 mV⁻¹) and a shorter
63 inactivation time constant (50 ms instead of 150 ms). The holding current to keep the resting membrane
64 potential at -60 mV was -30.826 pA for no I_A condition, 0 pA for I_A condition and -5.85 pA for I_A modified
65 condition. Spikes were induced by 3 ms positive current steps of 1 nA. Trains of spikes were induced by trains
66 of these current steps, at 40 Hz.

68 **Statistical analysis**

69 In many cases, we computed correlations between the different parameters characterizing the burst dynamics.
70 We generally computed and plotted the within cell correlations. Summary plots (mainly presented in Extended
71 Data) show, for each cell, the slope of the correlation (left part of the figure), the strength of the correlation (R
72 of the linear regression, right part of the figure). Single cell statistically significant correlations ($p < 0.05$,

73 corrected for multiple comparisons with the Bonferonni-Holm methods) are shown in dark blue (for both the
74 slope and strength of the correlation). Global population statistical analysis was performed on the slopes and
75 correlation coefficients of individual cells using standard t-tests, assessing that the population averages were
76 different from 0. Whiskers plots give minimum and maximal values (whiskers), second and third quartile (box),
77 and outliers calculated as deviations larger than $1.5 \times \text{IQR}$ (inter-quartile range) from the first and third quartiles
78 (diamonds). If not stated differently in results, the text gives the mean \pm 95% confidence interval (CI, defined as
79 $1.96 \times \text{SEM}$). Boxes show the mean and 95% confidence interval of the mean. Other quantities of interest are
80 effect sizes (ES), correlation coefficients (R), t-values (t) and p-values (p) of T-test on R values, and number of
81 cells used in the analyses (N). Note that p-values of T-test performed on slopes are only given in figures.
82 Bayesian analysis was performed with JASP (JASP Team (2020). JASP (Version 0.14.1) [Computer software]
83 by using the default effect size prior (Chauchy scale = 0.707).

84

85 **Exclusion criteria**

86 23 spontaneously active MCs were excluded from the analysis based on the following reasons: 5 showed poor
87 recording, 3 showed only continuous tonic activity, 11 showed too few bursts (< 4 bursts), 2 had too high
88 membrane resistance to be identified as MCs ($> 500 \text{ M}\Omega$), 2 presented burst intervals too short to compute
89 resting potential ($< 200 \text{ ms}$).

90

91 **Software**

92 All analyses were performed with custom Python 2.7 scripts, using the statistical or curve fitting functions from
93 Scipy 1.2.2, and the multiple comparison functions or multiple regression functions from StatsModels 0.9.0.

94

95 **Code accessibility**

96 Computational neuron model has been run with the software NEURON on a Linux personal computer. The
97 corresponding code is freely available at this address: <https://osf.io/9bgxp/>

98

99 **Data availability**

00 All raw electrophysiological traces, script for traces analysis, data analysis and models scripts are available at

01 Open Science Framework (<https://osf.io/s2dbw/>)

02

03

Results

Heterogeneity of spontaneous firing activity between different MCs

Whole cell recordings were performed on 72 spontaneously active MCs in olfactory bulb slices obtained from 21 rats aged between 30 and 42 days. Among recorded cells, 23 were excluded from the analysis based on criteria detailed in methods' section. As previously shown (Chen & Shepherd, 1997; Desmaisons et al., 1999; Balu et al., 2004), firing activity was characterized by clusters of APs, henceforth denominated bursts, separated by silent periods presenting subthreshold membrane oscillations (Fig 2A). A total of 1532 bursts (with at least 2 APs) and 386 isolated APs were analysed. Burst properties such as the number of APs, membrane potential at which bursts occurred, inter-burst frequency and intra-burst frequency were heterogeneous (Fig 2B, 2C, 2D and 2E; left). Such a heterogeneity could be partly due to specific differences among the recorded MCs (Fig 2B, 2C, 2D and 2E; right) which population shows intrinsic biophysical diversity (Padmanabhan & Urban, 2010), but also to the difference of the average holding potential (V_{rest}) between the different MCs. In fact, more depolarized MCs presented higher intra-burst frequency ($R = 0.58$, Wald test, $p < 0.001$, $N = 49$, not shown) and larger burst size (i.e. larger number of APs in burst, $R = 0.38$, Wald test, $p=0.007$, $N=49$, not shown). Burst size and intra-burst frequency ($R = 0.56$, Wald test, $p < 0.001$, $N = 49$, not shown) were also positively correlated. It should be noted that the V_{rest} distribution is bimodal (see methods) but because such a bimodality was not expressed in other burst parameters, all cells were pooled in subsequent analyses.

Dynamic modulation of AP threshold at resting potential

In cortical neurons, the AP threshold is affected by the trajectory of V_m that precedes the AP. In particular, when the V_m is hyperpolarized or the rate of membrane depolarization (dV_m/dt) preceding the AP is faster, a more negative AP threshold is observed (Henze & Buzsáki, 2001; Azouz & Gray, 2003; Li et al., 2014). Similarly, in MCs, the AP threshold is more negative when firing is preceded by V_m hyperpolarization induced by negative current injection (Balu et al., 2004). Interestingly, during spontaneous firing the initiation of a burst was ever preceded by a hyperpolarization of the V_m (see an example in Fig 3A-B), which is in agreement with a previous report (Desmaisons et al., 1999). We therefore investigated whether the oscillatory activity, potentially associated with the spontaneous inhibitory transmission, was capable to produce a dynamic modification of AP threshold contributing to the firing initiation. In MCs, the threshold of the first AP of a

33 burst was driven towards more negative values by a stronger hyperpolarization of V_m preceding the burst,
34 thereafter called pre-AP potential (see methods and Fig 1 for its calculation). The average modification of AP
35 threshold was of -0.37 ± 0.94 mV for 1 mV pre-AP potential hyperpolarization (ES = 1.13, R = 0.48 ± 0.08 , T-
36 test $t = 11.6$, $p < 0.001$, N = 49, Fig 3C). We then analyzed the depolarization rate of V_m preceding the first AP,
37 named here pre-AP slope (examples in Fig 3B; see methods and Fig 1 for its calculation). By contrast to what
38 was reported for cortical neurons and predicted by theoretical models (Platkiewicz & Brette, 2011), in MCs, a
39 larger pre-AP slope preceding the burst was associated to a more depolarized AP threshold (0.85 ± 0.71 mV
40 increase of AP threshold per 1 mV/ms increase of pre-AP slope; ES = 0.34, R = 0.18 ± 0.07 , T-test $t = 4.96$, $p <$
41 0.0001 , N = 49, Fig 3D). This unexpected effect may be a consequence of the small positive covariation we
42 measured between the pre-AP potential and the pre-AP slope (lower pre-AP slope for more hyperpolarized pre-
43 AP potential; average slope 0.04 ± 0.02 (mV/ms)/mV, ES = 0.52, R = 0.13 ± 0.07 , T-test $t = 3.41$, $p = 0.0013$, N
44 = 49, not shown). According to the literature, this covariation should induce opposite effects on the threshold
45 potential. Therefore, the pre-AP potential effect appeared to prevail on the pre-AP slope effect.

46 Since the AP threshold of MCs can dynamically shift depending on the recent history of V_m , it is conceivable
47 that the firing could be induced by hyperpolarizing events bringing the AP threshold below the median resting
48 potential (V_{rest} , see methods and Fig 1 for its calculation) or within the range of subthreshold V_m oscillations.
49 This was indeed the case for 27% of recorded bursts (representing 92 % of recorded MCs). Unsurprisingly the
50 level of hyperpolarization (pre-AP potential - V_{rest}) preceding the burst was larger in these cases (see example
51 in Fig 3E left) than in bursts where the threshold of the first AP remained above the V_{rest} (see example in Fig
52 3E right) (-1.30 ± 0.17 mV of hyperpolarization vs -0.56 ± 0.07 mV of hyperpolarization, T-test: $t = -9.48$, $p <$
53 0.001 , ES = 0.44, N = 513 and 1405, not shown). Altogether these data suggest that spontaneous firing in MCs
54 could be triggered according to two modalities: 1- a membrane hyperpolarization produced by the oscillatory
55 and/or inhibitory synaptic activity that bring(s) the AP threshold below V_{rest} or within V_{rest} variability (Fig 3E,
56 left); 2- a classical membrane depolarization above the V_{rest} , eventually produced by the excitatory synaptic
57 activity (Fig 3E, right).

58 Cellular mechanisms of AP threshold modification

60 The relationship between V_m and AP threshold was further investigated in experiment depicted in Fig 4. Here
61

62 MCs were slightly hyperpolarized with a steady current injection to prevent spontaneous firing and 2 successive
63 APs were evoked at 6 second intervals by short (3 ms) depolarizing current steps; the second AP being preceded
64 by 50 ms hyperpolarizing current step (Fig 4A, left). The comparison of AP thresholds between the two evoked
65 APs showed that pre-AP membrane hyperpolarization produced a linear shift of AP threshold toward more
66 hyperpolarized values (-0.32 ± 0.05 mV threshold shift per each mV of membrane hyperpolarization; Fig 4A,
67 right, $N = 75$). The same effect was obtained with pre- AP hyperpolarization duration varying over a range from
68 10 to 90 ms (Fig 4B, $N = 16$). The contribution of the membrane depolarization rate to AP threshold was
69 evaluated by comparing the effect of depolarizing ramps at different speeds (Fig 4C, left). For the recorded MCs
70 ($N = 11$), faster depolarization rate leads to more negative AP thresholds (Fig 4C, right). The slope of the linear
71 regression obtained from AP threshold/ depolarizing speed analysis showed a shift of AP threshold of -7 ± 3 μ V
72 for each mV/ms of membrane depolarizing speed (Fig 4C right; $ES = -1.2$ $p = 0.003$). Therefore, similarly to
73 what was observed in cortical neurons (Henze & Buzsáki, 2001; Azouz & Gray, 2003; Li et al., 2014), AP
74 threshold in MCs became more negative when V_m was depolarized with a fast depolarization rate. This result
75 supports the interpretation that the opposite correlation between AP threshold and pre-AP slope during
76 spontaneous firing (shown in Fig 3D) would be a consequence of a more hyperpolarized pre-AP potential when
77 the pre-AP slope is lower.

78 The most likely mechanism responsible for the modification of threshold produced by membrane
79 hyperpolarization is the recovery from inactivation of voltage dependent channels implicated in AP generation;
80 namely, the Na^+ and T-type Ca^{2+} channels. To test this assumption, we used the same experimental procedure as
81 described in Fig 4A, combined with a pharmacological approach as well as a computational neuron model.
82 Since the pharmacological compounds were applied at different time periods, we first assessed that the effect of
83 membrane hyperpolarization on AP threshold effect was stable over time by testing it 5 min and 10 minutes
84 after the beginning of the recording (Extended Data Fig 5-1 C-D). To investigate the effect of the recovery from
85 inactivation of Nav channels on AP threshold decrease, we first used a simple computational neuron model
86 containing only one Nav channel type and one Kv delayed-rectifier channel type (see methods for details). This
87 model well mimicked the shift of AP threshold produced by the membrane potential hyperpolarization (Fig 5A).
88 Thus, the shift could be attributable to the recovery from inactivation of Nav channels produced by the V_m
89 hyperpolarization, leading to a hyperpolarization of AP threshold. To observe the effect of partial blockade

90 of Nav channels, we decreased the density of Nav channels to $50 \text{ pS}/\mu\text{m}^2$ and $25 \text{ pS}/\mu\text{m}^2$. As expected,
91 decreasing the density of Nav channels in the model, led to a shift of AP threshold toward more positive values
92 (Fig 5B). More interestingly, under reduced Nav condition (50 and $25 \text{ pS}/\mu\text{m}^2$), the hyperpolarization of
93 membrane potential resulted in a larger decrease of AP threshold than in control condition (Fig 5B, note that the
94 slope of the curve hyperpolarization/threshold shift became larger with the decrease of Nav channels density).
95 This can be explained by taking into account that AP threshold is not linearly correlated with the quantity of
96 activatable Nav channels. Fig 5C shows the curve of the AP threshold vs quantity of activatable Nav
97 conductance, just before the AP occurrence. On this curve, we plotted: the quantity of Nav conductance
98 activatable at V_{rest} (-60 mV) or after 10 mV hyperpolarization (-70 mV) for the 3 conditions of Nav channels
99 density ($200 \text{ pS}/\mu\text{m}^2$ in red, $50 \text{ pS}/\mu\text{m}^2$ in green or $25 \text{ pS}/\mu\text{m}^2$ in blue). We can see that the increase of Nav
00 channels availability, produced by V_{m} hyperpolarization, is associated with a greater decrease of AP threshold
01 in reduced Nav condition ($50 \text{ pS}/\mu\text{m}^2$ or $25 \text{ pS}/\mu\text{m}^2$) than in control condition ($200 \text{ pS}/\mu\text{m}^2$). The prediction of
02 the model was checked by applying low doses of the Na channel blocker, TTX (10 or 20 nM). The availability
03 of Nav channel was reduced by TTX at these doses, as assessed by the positive shift of AP threshold (Extended
04 Data Fig 5-1B). In agreement with the model prediction, the effect of membrane hyperpolarization on AP
05 threshold was amplified by TTX at 20 nM (Fig 5D; difference between threshold/hyperpolarization slopes in
06 control and TTX 20 nM : $0.26 \pm 0.18 \text{ mV/mV}$, $ES = 0.6$, $p = 0.01$, $N = 22$). Interestingly, this effect was not
07 observed with TTX at 10 nM (Fig 5E; difference between threshold/hyperpolarization slopes in control and
08 TTX 10 nM : $-0.03 \pm 0.18 \text{ mV/mV}$, $ES = -0.16$, $p = 0.48$, $BF_{10} = 0.3$, 'evidence of absence', $N = 19$). This result
09 suggests that, around -60 mV , the recovery from inactivation produced by the hyperpolarization would mainly
10 involve the Nav channel sub-types blocked at $[TTX] > 10 \text{ nM}$ (see discussion). The participation of T-type Ca^{2+}
11 channel was also investigated by using the selective antagonist ML218 (5 - $10 \mu\text{M}$). As shown in Extended Data
12 Fig 5-1 E, ML218 did not modify the shift of AP threshold induced by membrane hyperpolarization (difference
13 between threshold/hyperpolarization slopes in control and ML218: $-0.0 \pm 0.1 \text{ mV/mV}$, $ES = 0.1$, $p = 0.66$; $N =$
14 21), indicating that this effect was not based on recovery from inactivation of T-type Ca^{2+} channels. We finally
15 determined whether, in MCs recorded close to V_{rest} (-60 mV), short hyperpolarization of V_{m} could produce a
16 recovery from inactivation of Na^+ channels. To this end, we performed the experiment depicted in Fig 5F. Here,
17 Na^+ current was pharmacologically isolated (see methods) and MCs were recorded in voltage clamp

18 configuration. Following the short membrane prehyperpolarization (25 ms), the amplitude of Na^+ current
19 generated by a 5 ms depolarization step to -10 mV, increased proportionally to the hyperpolarization level
20 ($p=0.0002$, $N=6$, Friedman test). Moreover, the recovery from inactivation of Na^+ channels was independent of
21 the duration of the hyperpolarization, in the 10 to 90 ms range, ($p = 0.74$, $N=6$, Friedman test). These results
22 echoed the effects produced by membrane hyperpolarization on AP threshold that were depicted in Fig 4A and
23 4B, further supporting the hypothesis that the threshold shift was based on the recovery from inactivation of Na^+
24 channels.

25 **Spontaneous bursting activity was promoted by dynamic modification of AP threshold induced by AHP**

26 We next investigated the impact of dynamic modifications of AP threshold on MC firing during the burst. As
27 shown in Figure 6A, the AP thresholds within the bursts were naturally shifted to more negative potentials than
28 those of the first AP (delta difference of threshold between the first and second AP in the burst = -2.28 ± 0.09
29 mV, $N = 1532$ bursts, $ES = -1.28$, T-test $t = -50.0$, $p < 0.001$, see Figure 6B). The most likely explanation of the
30 threshold shift within the burst is the membrane hyperpolarization induced by the preceding AHP. Indeed, the
31 modification of AP threshold shift, calculated between the first and the second AP of the bursts, positively
32 correlated with the AHP amplitude, measured here relatively to the first pre-AP potential (-0.35 ± 0.10 mV of
33 AP threshold shift for each mV of membrane hyperpolarization, Fig 6C left), as well as with the repolarization
34 rate of the AHP (-5.6 ± 1.5 μV of AP threshold shift for each mV/s of modification of membrane depolarizing speed, Fig
35 6C right). These results suggested that both the AHP amplitude and repolarization rate accounted for the negative AP
36 threshold shift within the burst. Interestingly this effect, observed at the single cell level, was also seen at the population
37 level, by looking at average values per cell (see Extended Data Fig 6-1 C and D). Once the first AP fired from resting
38 potential, the AP threshold shift, induced by AHP, could act as a regenerative mechanism of firing, especially
39 when it drove the threshold below the V_{rest} (Fig 6A left) or within the range of spontaneous membrane
40 oscillations (Fig 6A middle). To precisely assess the position of AP thresholds relatively to subthreshold
41 fluctuations, we normalized the thresholds of intra-burst APs (i.e. all the APs except the first one) using a linear
42 interpolation. We set V_{rest} at 0 and, the maximum amplitude of the subthreshold fluctuations, at 1. We called
43 this measure “normalized relative AP threshold”. In such conditions, a negative value for the normalized AP
44 threshold meant that it was more hyperpolarized than V_{rest} , a value between 0 and 1, meant that it was within
45 the range of V_m intrinsic subthreshold fluctuations and, a value above 1, meant that it was more

46 depolarized than subthreshold fluctuations. As shown in Fig 6D, AP threshold was more negative than V_{rest} for
47 39 % of intra-burst APs: it remained within the range of subthreshold membrane oscillations for 52 % and,
48 above membrane oscillatory activity, for the remaining 9 %. A clear heterogeneity of the normalized relative AP
49 threshold was observed between MCs (see Extended Data Fig 6-2A). Interestingly the AP threshold shift
50 relative to the V_{rest} (relative AP threshold), appeared to affect bursts properties. Stronger negative shifts were
51 associated to burst having higher numbers of APs (Fig 6E left) and higher intra-burst firing frequency (Fig 6E
52 right). A similar correlation was observed between the average intra-burst AP relative threshold in different
53 MCs and their average bursts size and intra-burst frequency (see Extended Data Fig 6-2 C).

54 As expected from the relationship between the AHP and AP threshold shift, the intra-burst firing properties
55 correlated with AHP properties. Larger AHP amplitudes were associated to longer bursts and higher firing
56 frequencies (see Extended Data Fig 6-3 A1 and B1). In addition, faster AHP repolarizations were associated to
57 longer bursts and higher firing frequencies (see Extended Data Fig 6-3 C1 and D1). We also observed that the
58 speed of repolarization of AHP more strongly impacted MC firing properties than AHP amplitude. Similar
59 contribution of AHP to MC firing properties was observed when performing between-cells analyses (see
60 Extended Data Fig 6-3, panels A2, B2, C2, D2); suggesting that firing heterogeneity between the different MCs
61 reported in Fig 1 are, at least partly, based on the heterogeneity of their AHP characteristics with a predominant
62 role of the AHP slope.

63 By using electrical stimulation of the olfactory nerve, synaptically evoked firing was induced in two MCs. As
64 shown in Extended Data Fig 6-4, the evoked-firing induced bursts in these cells had similar properties to
65 spontaneous ones, except that subthreshold EPSP lasted longer than the AP duration. These preliminary results
66 suggest that, once APs are generated, the bursting characteristics of MCs are determined by their intrinsic
67 biophysical properties, i.e. the AHP, regardless the modality of AP induction.

68 So far, we provided evidence that the frequency and spike number of MC bursts were affected by the negative
69 shift of AP threshold produced by the AHP, through the recovery from inactivation of Na^+ channels. However,
70 the burst properties depend also on the V_{rest} . In fact, the frequency and spike number of MC bursts were
71 increased when V_{rest} was depolarized (Fig 7). This effect was likely due to the stronger negative shift of AP
72 threshold within the burst when the V_m was depolarized (see Extended Data Fig 7-1C). Three factors could
73 support the latter effect: 1 - an increase in AHP amplitude with V_m depolarization (Extended Data Fig

74 7-1D); possibly due to the increase in K^+ driving force with the membrane depolarization; 2 - an increase in
75 AHP repolarization speed of the AHP with V_m depolarization (Extended Data Fig 7-1E); 3 - a stronger effect of
76 Nav channels recovery from inactivation, due to increased steady-state-inactivation when the V_m was
77 depolarized. Indeed, in the simple neuron computational model, a depolarization of the V_m led to a partial
78 inactivation of Nav channels, a reduction of the quantity of pre-spike activatable Nav channels and therefore a
79 greater effect of V_m hyperpolarization on AP threshold shift (Extended Data Fig 7-1 G, H). The third factor is
80 experimentally supported by the observation that the slope of the correlation between relative AP threshold and
81 AHP amplitude was larger for depolarized MCs (i.e., for a same AHP amplitude, AP threshold negative shift is
82 larger for depolarized V_m) (Extended Data Fig 7-1F). Overall, the three factors could cooperate to make the
83 relative AP threshold more negative, thus making the bursts longer and faster for the more depolarized V_m . All
84 these effects, shown here at the cellular level were also observed at the population level (cell-to-cell analysis,
85 not shown).

87 **The evolution of the late slow component of the AHP contributed to the burst termination**

88 A plausible mechanism that could account for the burst termination is the evolution of the AP threshold along
89 the burst bringing this parameter above the V_{rest} . However, although a small positive shift of the AP threshold
90 was observed along the bursts (Fig 8A left, increase of normalized threshold: mean 0.053 ± 0.027 mV, paired t-
91 test: $t = 3.83$, $p < 0.001$, $N = 1276$, $ES = 0.11$), the AP threshold remained largely below, or within, the range of
92 V_m subthreshold oscillation (Fig 8A right). The small evolution of AP threshold probably reflected the small
93 decrease of absolute AHP amplitude and small slowing-down of AHP repolarization rate along the bursts (see
94 Extended Data Fig 8-1). To further clarify the mechanisms of burst termination we used a linear model (using
95 V_{rest} , AHP amplitude, AHP slope and AHP duration as parameters, see methods for details) which predicts the
96 dynamics of putative AP threshold after the last AP of the burst (see examples in Fig 8B, red dashed lines). This
97 analysis showed that, for 89% of the bursts, the V_m that followed the last AP did not overcome the putative
98 threshold (Fig 8C left). Such an effect cannot be explained by an overestimation of the threshold by the model
99 since, at a time interval equal to the last inter-spike interval, the predicted threshold was similar to the threshold
00 of the last AP of the burst (Fig 8C right, difference of potential between last AP threshold and predicted
01 threshold: 0.09 mV, $SD: 0.68$ mV, $N = 1532$ bursts). Indeed, the failure of V_m to overcome the AP threshold

02 appears to be due to the modification of the AHP, in which a late, slow repolarizing component develops
03 following the early fast repolarizing component characterizing the intra-burst AHP. This new AHP component
04 could be fitted with a slow exponential (time constant: mean: 171.66 ms, SD: 88.76 ms, N = 42 MCs, Fig 8D-E,
05 see also Fig 2C in Balu and Strowbridge, 2004). This component kept the V_m more hyperpolarized than during
06 the intra-burst AHPs, preventing the V_m to reach the AP threshold. This result suggests a scenario where the AP
07 threshold can only be reached during the early fast component of the AHP repolarization phase, with the onset
08 of the late slow AHP repolarization preventing the V_m from reaching a threshold moving rapidly to pre-burst
09 values.

10 Thus, the termination of burst discharge seems to be attributable to the onset of a slow component during the
11 repolarizing phase of the AHP. In order to investigate how this slow component develops along the burst, we
12 performed the experiment depicted in Fig 9. Here MCs were slightly hyperpolarized with a steady current
13 injection, preventing spontaneous firing, while trains of APs were evoked by short (3 ms) depolarizing-current
14 steps at 40 Hz. Five trains of 1, 2, 4, 8 and 16 APs respectively, were generated and the parameters of the last
15 AHP were compared (Fig 9A). As shown in Fig 9C-D the AHP amplitude and area increased with the number
16 of APs (repeated measures ANOVA $p < 0.001$, N = 11). Interestingly, the slow AHP component appeared at
17 more and more hyperpolarized V_m as the number of APs increased (repeated measures ANOVA $p < 0.001$, N =
18 11, Fig 9E). This result suggests that, in spontaneous bursts, the probability that the fast AHP repolarizing
19 component can overcome the AP threshold decreases along the AP sequence until it is no longer able to produce
20 further APs. The slow late AHP component is reminiscent of the slow inactivating K^+ current that was
21 previously observed in MC following membrane hyperpolarization and that was suggested to be produced by
22 the recovery from inactivation of I_A current (See Fig 5 of Balu & Strowbridge, 2007). The hypothesis that the
23 slow AHP component is due to the deinactivation of the I_A current during fast AHP is further supported by a
24 computational model of MC showing this current increases during the AP burst (Rubin & Cleland, 2006).
25 Indeed, application of 4AP (3 mM, Fig 9B) prevented the evolution of AHP during the evoked AP trains (AHP
26 area: 4AP effect $p = 0.005$; interaction $p < 0.001$; AHP amplitude: 4AP effect $p = 0.002$; interaction $p < 0.001$;
27 Fig 9C-D) as well as the negative shift of V_m at which the slow AHP component appears, (4AP effect $p=0.004$;
28 interaction $p<0.001$; Fig 9E). Note that 4AP reduced both the early-fast and late-slow AHP. The hypothesis that
29 the slow component involves the activation of I_A current is further supported by our neuron model (Fig

30 9F). In fact, in the simple model involving only Nav and Kdr channels, there was no development of a slow
31 AHP component when the number of APs increased (Fig 9F left, no I_A). However, the implementation of I_A
32 current to the model reproduced the development of a slow AHP with the number of APs, as observed in our
33 recordings (Fig 9F, I_A and I_A modified). The conductance of I_A was either directly taken from (Rubin & Cleland,
34 2006) or modified, to get biophysics closer to previously published I_A biophysics (Amendola et al., 2012) (see
35 methods). Noteworthy is that the I_A current is minimal at the AHP peak and then increases again during the
36 repolarization phase of the fast AHP, leading to the development of the slow AHP component (Fig 9F, lower
37 panels). Altogether these data suggest that, in MCs, the burst is stopped by the build-up of 4-AP-dependent I_A -
38 like current that, by slowing down the AHP, brings the AP threshold to values that cannot be reached during V_m
39 repolarization.

40
41
42 **The fast AHP features from the first spike of the burst and slow AHP dynamics are informative about**
43 **intra-burst frequency and burst size.**

44
45 Altogether, our experiments suggested that, in MCs, the burst frequency is determined by the fast AHP
46 component while the burst termination (and thus the burst size) is determined by the development of the slow
47 AHP during the burst. Therefore, we decided to observe if the features of the fast and slow AHP, measured
48 respectively after the first and the last AP of the burst, are good predictors of burst dynamics.

49 First we only considered V_{rest} and fast AHP features. Pooling data from all cells (but only from bursts with at
50 least 3 APs), we used linear models to predict burst size (number of APs) and within burst frequency based on:
51 V_{rest} , fast AHP amplitude and fast AHP depolarization rate measured after the first AP of each burst (see
52 methods for model details). The models showed that burst frequency clearly depends on all parameters and their
53 interactions ($R^2 = 0.69$, $F_{10,1081} = 410.9$, $p < 0.0001$, $N=1092$ bursts). A similar but smaller effect was observed
54 for burst size ($R^2 = 0.27$, $F_{10,1081} = 66.3$, $p < 0.0001$, $N=1092$ bursts). Thus, fast AHP dynamics following first
55 AP is more informative of burst frequency than burst size.

56 Then, we also considered slow AHP features by introducing, in the linear models, the average time constant of
57 the slow AHP (measured once in each cell, see Fig 8E). It should be noted that what we expected to be
58 important in controlling the burst termination was the development of the slow AHP during the successive APs

59 of the burst but, this could not be measured from the traces of spontaneous bursting activity. We therefore
60 assumed that the development of the slow AHP correlated with its average time constant which we could
61 measure at the end of the burst. The addition of the mean time constant of the slow AHP to the linear model
62 independent variables significantly improved their fitting performance, in particular on burst length (ANOVA
63 comparisons of models with and without the time constant of the slow AHP as parameter: frequency: $F_{4,1081} =$
64 28.6, $p < 0.0001$; burst size: $F_{4,1081} = 25.5$, $p < 0.0001$; R^2 of the new linear models and effect size f^2 between
65 models: frequency: $R^2 = 0.72$, $f^2 = 0.03$; burst size: $R^2 = 0.33$, $f^2 = 0.06$).

66 Overall the linear model analysis confirmed that the burst properties largely depend on the characteristics of the
67 initial fast AHP and V_{rest} , the slow AHP impacting the termination of the burst and thus, the burst size.

68 69 70 71 72 73 74 75 76 77 78 79 80 81 82 83 84 85 86 87 88

Discussion

Our study provides new insights into the understanding of the intrinsic cellular mechanisms responsible for the
genesis of firing activity in MCs. More precisely, we have shown that AHP plays a key role in this genesis since
changes in its characteristics (duration, amplitude, kinetics) can both trigger and stop the burst generation while
also determining the bursting properties. The experimental results presented in this report have been synthesized
to build the toy model described in Fig 10. The firing of MC is triggered by a modification of the AP threshold
that dynamically changes as a function of the V_m trajectory (Fig 10A). Due to the relatively depolarized V_{rest}
of MCs, a part of the voltage dependent Na^+ channels are inactivated. Hyperpolarization of V_m due to intrinsic
oscillatory activity and/or synaptic inputs leads to Na^+ channels deinactivation, bringing the AP threshold
within V_m subthreshold fluctuations, thus, facilitating the firing. Once the first AP is generated, the following
fast AHP brings the threshold below the V_{rest} , or within the V_{rest} noise, acting in this way as a regenerative
mechanism that will produce the burst (Fig 10B). The burst termination is ensured by a slow, 4AP dependent,
AHP component that progressively develops along the consecutive APs, and is hypothesized to involve I_A

89 current. This component slows down the AHP repolarization phase, thus increases the inactivation of Nav^+
90 channels and moves back the AP threshold to values that cannot be overcome by V_m repolarization. The intra-
91 burst properties (frequency, length) are determined by the magnitude of the modification of AP threshold
92 relative to the V_{rest} . The larger the modifications of AP threshold, the larger the bursts (in terms of number of
93 APs) and the higher intra-burst firing frequencies (Fig 10 C). Indeed, the firing frequency increases because the
94 AP threshold is reached faster during the AHP repolarization phase, especially when the shift of the AP
95 threshold towards hyperpolarizing values is associated with faster AHP repolarization. Besides burst size
96 increases because the AHP slow component needs more APs in order to manifest itself at V_m , more negative
97 than the AP threshold (Fig 10 B middle and lower panels). Finally, because the shift of the AP threshold during
98 the burst is driven by the AHP, the burst properties are determined by the AHP features. In particular, the
99 number of APs and firing frequency increase, when the AHP amplitude and repolarization rate increase. The
00 model also predicts the increases of burst length and intra-burst frequency that we observed upon membrane
01 depolarization (Fig 10D). In this condition the AHP amplitude increases, possibly due to an increase of K^+
02 driving force and, the AHP repolarization becomes faster, by a yet unknown mechanism. Moreover, upon
03 membrane depolarization, the number of inactivated Nav channels augments. As a consequence, the recovery
04 from inactivation of Nav channels produced by the AHP entails a larger shift of AP threshold relative to V_{rest} .
05 In fact, our neuron computational model showed that a decrease of the number of Nav channels available,
06 entails an increase of the hyperpolarization-induced AP-threshold shift (Fig 5C-D and Extended Data Fig 7-1 G-
07 H).

08 Altogether, the heterogeneity of the firing properties observed among the different MCs would therefore be
09 mainly due to differences in shape of their AHP components, as well as the recent history of V_m values.

10 However, our model does not predict the minority of intra-burst APs for which the threshold was clearly above
11 the V_{rest} (Fig 6A right). A mechanism that could account for these events is the rebound depolarization that was
12 frequently observed at the end of the AHP. Obviously when it could be detected, the rebound depolarization did
13 not overcome the AP threshold, but a great variability in the rebound amplitudes was observed, supporting the
14 above hypothesis. The post-AHP rebound depolarization is possibly due to the activation of persistent Na^+
15 current (Balu & Strowbridge, 2007).

16 Not only depicting our own results, our model fits with others reported in the literature. As an example the

17 tufted cells of the olfactory bulb, that present an AHP with larger amplitude and faster repolarization rate than
18 MCs, show a more sustained bursting activity; namely longer and higher frequency bursts (Burton & Urban,
19 2014). Similar covariation between AHP and burst properties have been also reported in MCs during postnatal
20 development (Yu et al., 2015). Our model predicts that these covariations are the consequence of AHP
21 dependent modifications of the AP threshold shifts. In agreement with our hypothesis of the involvement of I_A
22 current in burst termination, the application of 4AP, has been reported to transform MC bursting activity into a
23 continuous firing one (Balu et al., 2004). MCs present a dendritic recurrent synaptic transmission that is
24 characterized by a glutamatergic auto-excitation (Aroniadou-Anderjaska et al., 1999; Friedman & Strowbridge,
25 2000; Salin et al., 2001) and a feed-back inhibition that follows the activation of granular cells (Isaacson &
26 Strowbridge, 1998; Schoppa et al., 1998). It has been shown that the main effect of recurrent synaptic
27 transmission is to shape the AHP of MC (Duménieu et al., 2015). In particular, the recurrent inhibition increases
28 the amplitude of the AHP without affecting the medium or the late AHP, while the recurrent excitation reduces
29 both the amplitude and the medium component of the AHP (see Duménieu et al., 2015 Fig 5D). Based on the
30 present results we can therefore propose that recurrent synaptic inhibition would favor long bursts at higher
31 firing frequency; by contrast, the functional role of recurrent excitation is less predictable. Indeed, while the
32 reduction of the AHP amplitude would favor short bursts at low frequency, we do not know whether and, to
33 what extent, the reduction of medium component would affect the velocity of the repolarization phase of the
34 AHP and, further analysis on this aspect is needed to elucidate the role of recurrent excitation on MC firing
35 properties.

36 The interpretation of some of our experimental results requires further discussion: in particular, the contribution
37 of I_A in the AHP course (Fig 9) and the role of the recovery of sodium channel in the modification of AP
38 threshold (Fig 5). As evidenced from Fig 9, an increase in AHP amplitude was observed when the number of
39 evoked consecutive APs increased. This appeared as mainly based on the increase of 4AP-dependent AHP-
40 component. Noteworthy was that during spontaneous bursts we did not observe any increase of AHP amplitude
41 (Extended Data Fig 8-1A). One possible explanation is that I_A develop earlier when the APs are evoked by
42 experimental depolarizing steps; the later having a long duration (3 ms), relatively to the AP half width (~ 0.7
43 ms). Moreover, the depolarizing step could mask the actual starting point of the AHP, giving the impression that
44 I_A component was already present since its beginning. It is therefore plausible, that during spontaneous firing

45 activity I_A appears early enough to affect the medium/slow AHP, and therefore slows down the AHP
46 repolarization during the burst, but too late to affect the amplitude of the AHP. The hypothesis of the
47 involvement of the recovery from inactivation of Nav in threshold modifications implies an increase of the
48 effect of hyperpolarization when the global availability of Nav channels is reduced (Fig 5C-D). This was
49 confirmed by the application of TTX at 20 nM but not when TTX at 10 nM was used. However, TTX 10 nM
50 application is enough to reduce the Nav channels availability as the AP threshold was shifted positively in this
51 condition (Extended Data Fig 5-1). The absence of the effect with TTX at 10 nM is probably not a consequence
52 of sampling variability (i.e. a false negative result) since Bayesian analysis supports an actual absence of the
53 effect ($BF_{10} < 1/3$; Keyzers et al 2020). Moreover, when selecting only neurons for which both 10 and 20 nM
54 TTX were applied, 20 nM reliably increased the effect of the Vm hyperpolarization on AP threshold while 10
55 nM did not (data not shown). A plausible interpretation of these results is that the recovery from inactivation -
56 produced by membrane hyperpolarization- may involve only those of the different sub-types of Nav channels
57 having a low sensitivity to TTX, thus not yet blocked at 10 nM. Further investigations are needed to confirm
58 such a hypothesis, for example, by using selective antagonists of the different Nav subtypes.

59 Lastly, our extensive analysis of the mechanisms that govern the discharge properties of MCs leads to the
60 question of the functional significance and impact of these properties. The heterogeneity of the firing properties
61 reported here confirmed previous reports of MC recordings *in vivo* et *in vitro* (Rinberg et al., 2006;
62 Padmanabhan & Urban, 2010; Kollo et al., 2014; Leng et al., 2014). It has been proposed that such a diversity
63 reduces the correlation of firing between different MCs to a correlated input, in this way increasing the
64 information content of MC population activity (Padmanabhan & Urban, 2010). Moreover, computational
65 simulations suggest that MC firing heterogeneity allows a more efficient and robust coding of stimulus
66 information (Tripathy et al., 2013) and increases the synchronicity of MC firing when the correlation between
67 the inputs is low, by possibly promoting encoding of odour combinations acting on different types of sensory
68 receptors (Zhou et al., 2013). Our results show that the diversity among the population of MCs is largely
69 determined by the heterogeneity of the AHP characteristics which play a pivotal role in determining the
70 properties of MCs' firing activity. However, the AHP characteristics can be directly altered by the membrane
71 potential (present work), neuromodulation (Wu et al., 2002; Brosh et al., 2006), postnatal development
72 (Duménieu et al., 2015 ; Yu et al., 2015), learning (Duménieu et al., 2015; Reuveni & Barkai, 2018) and

73 recurrent synaptic transmission (Duménieu et al., 2015). Therefore, thanks to highly scalable characteristics, the
 74 AHP appears to be a key target for the modulation of olfactory bulb processing according to many parameters
 75 such as physiological state (reproduction period, food need, etc), memory and experience.

76 **Figure legends:**

77 **Figure 1: Schematic description of the main measurements performed on spontaneous bursts during the**
 78 **study.** Red dots represent the thresholds of APs. Purple diamonds represent the most hyperpolarized value of
 79 V_m before one given spike (namely “pre-AP potential” before first AP and “AHP peak” before the other APs)

80

81 **Fig 2: Burst properties of MCs. A:** Left, example of spontaneous recording in MCs showing typical bursts of
 82 APs. APs belonging to the same burst are alternatively identified by red and green stars. Right, enlargement of
 83 the trace in A left showing V_m dynamics with fast oscillations which were typical during inter-burst periods. **B:**
 84 Distribution of V_m values preceding bursts (V_{rest}) **Left:** distribution for all detected bursts, **Right:** whisker plot
 85 per cell showing inter-cell variability). **C:** Distribution of burst sizes (number of APs in bursts, left and right:
 86 same representation as in B). **D:** Distribution of inter-burst intervals (same representation as in B). **E:**
 87 Distribution of intra-burst frequencies (left and right: same representation as in B). In left panels (B-E),
 88 continuous and dashed vertical lines materialize the mean and median values respectively. Diamonds in right
 89 panels (B-E) represent outliers calculated as deviations larger than $1.5 \cdot IQR$ (inter-quartile range) from the
 90 first and third quartiles.

91

92 **Fig 3: The threshold of the first AP of the burst is affected by the V_m trajectory before threshold. A:** Burst
 93 were often initiated after a hyperpolarization phase of the V_m (pre-AP potential). Here, V_m traces preceding
 94 each burst of a single neuron (#32) were averaged (blue line) along with their STD (shaded area). **B:** Example
 95 of the variability of pre-AP slope and first AP threshold in the same cell (neuron #32). For each trace, a
 96 diamond marks the pre-AP potential, a round dot, the first AP threshold and a dashed line, the pre-AP slope
 97 (lines are displayed in the time interval where V_m was fitted). Each color corresponds to one given trace. Note
 98 that a more negative threshold value corresponds to a more hyperpolarized pre-AP potential. See methods and
 99 Fig 1 for the details of each measure. **C:** AP threshold positively correlated with pre-AP potential. Left panel,
 00 correlations between the pre-AP potential and first AP threshold. A linear fit was done for each neuron (one dot
 01 per burst, the fit is shown as a black line). In purple the measurements and fit of the neuron exemplified in
 02 panels A-B. Average slope and average correlation across neurons are displayed above (mean \pm sem, $N = 49$
 03 MCs). Right panels: scatter plots of the slopes (left) and correlation coefficients (right) obtained from the linear
 04 fit done for each neuron in the left panel. Darker dots correspond to individual fits with $p < 0.05$ (Pearson
 05 correlation, corrected for multiple comparisons). Black boxes show the mean and its 95% confidence interval
 06 for each distribution. The significance of deviation from 0 of each distribution was further tested with a one
 07 sample t-test (p -values are displayed above each scatter plot, see main text and methods for additional details).
 08 **D:** Small positive correlation between the V_m slope preceding the first burst AP (pre-AP slope) and first

09 AP threshold. Data are presented as in C. **E:** Left: examples (black and grey lines) of strong membrane
 10 hyperpolarization bringing the AP threshold (large dots) within the range of membrane fluctuations. Right:
 11 examples of AP threshold that remained above membrane fluctuations. For comparison, traces were aligned on
 12 V_{rest} (set at 0 for the figure). All four examples come from the same recording (neuron #24).

13
 14 **Fig 4: AP threshold of MCs decreased with membrane hyperpolarization and high depolarization speed. A:**
 15 AP threshold decreased proportionally with membrane hyperpolarization. Left; experimental protocol and
 16 representative example of threshold modification by membrane hyperpolarization. Dots show AP thresholds,
 17 dashed line shows the threshold position in absence of hyperpolarization. Right; quantification of spike
 18 threshold modifications produced by membrane hyperpolarization. Inset; analysis performed on the neuron
 19 150403a depicted on the left. The number of cells is given below each point. **B:** Spike threshold modification
 20 was not affected by the duration of membrane hyperpolarization. Upper; schematic representation of the
 21 experimental protocol. Bottom; quantification of the effect ($N = 16$ MCs). Black circles: average AP threshold
 22 modification; grey diamonds: average membrane hyperpolarization (same scale than threshold modification).
 23 **C:** AP threshold decreased with the membrane depolarization rate. Upper; experimental protocol and
 24 representative examples of AP thresholds for different depolarization rates. Stars show the threshold position;
 25 lower lines materialize depolarization current ramps (only the last 10 ms preceding the threshold is shown).
 26 Bottom; quantification of AP threshold as a function of membrane depolarization rate for 11 MCs. Inset:
 27 quantification of AP threshold modification as a function of membrane depolarization rate for the 11 MCs. ES
 28 = effect size. Horizontal and vertical bars represent 95% Confidence Interval.

29
 30 **Fig 5: Sodium but not calcium channels participate to the modification of the AP threshold induced by**
 31 **membrane hyperpolarization. A:** Neuron model simulation showing the modification of AP threshold with
 32 membrane hyperpolarization for high Nav density ($200 \text{ pS}/\mu\text{m}^2$) and low Nav density ($50 \text{ pS}/\mu\text{m}^2$). Lower
 33 panels are enlargements of upper panels. AP thresholds are marked by black dots. **B:** Quantification in the
 34 neuron model of the effect of membrane hyperpolarization on AP threshold for different Nav channels densities.
 35 Note an amplification of the AP threshold shift induced by membrane hyperpolarization when the density of Nav
 36 channels was reduced. **C:** Curve depicting the modification of AP threshold in the neuron model as a function of
 37 the quantity of Nav conductance activatable before the AP. Note that the same 10 mV membrane
 38 hyperpolarization produced a stronger modification of AP threshold when the density of Nav channels was
 39 reduced (compare the 3 conditions: $200 \text{ pS}/\mu\text{m}^2$, $50 \text{ pS}/\mu\text{m}^2$, $25 \text{ pS}/\mu\text{m}^2$) **D:** TTX at 20 nM amplified the AP
 40 threshold shift induced by membrane hyperpolarization ($ES = \text{effect size}$). **E:** TTX at 10 nM failed to amplified
 41 the AP threshold shift produced by membrane hyperpolarization $ES = \text{effect size}$. **F:** Membrane
 42 hyperpolarization resulted in an amplification of Na^+ current in MCs. High left; experimental protocol
 43 depicting the imposed modifications of membrane voltage. High right, representative of Na^+ current following
 44 membrane hyperpolarization. Low left, quantification of the modification induced by different levels of
 45 membrane hyperpolarization on Na^+ current amplitude. Low right, quantification of the modification produced,

46 by different duration of membrane hyperpolarization, on Na^+ current amplitude. * $p < 0.02$; ** $p < 0.01$; *** p
 47 < 0.001 ; post hoc comparisons with the condition without hyperpolarization, Dunn's test. Bars represent 95 %
 48 CI in A,E,F and s.e.m in G. **More details on pharmacological protocol, time stability of AP threshold and**
 49 **effect of VDCC antagonist can be found in Extended Data (extended data figure 5-1).**

50 **Fig 6: The AHP induced hyperpolarization lowered the AP threshold within the bursts and determine the**
 51 **firing properties.** **A:** examples illustrating the lowering of threshold for APs within the burst. Dashed line is
 52 V_{rest} . Note that in left and middle panels AP threshold is shifted below V_{rest} or inside V_m fluctuations
 53 respectively. In right panel the rebound of V_m observed after the AHP could potentially allow the burst
 54 generation despite the high AP threshold relative to V_{rest} . **B:** histogram of differences of AP threshold between
 55 the second and the first AP of the bursts. **C:** AHP properties determine the negative shift of AP threshold. Left,
 56 larger AHP produced larger negative shift of AP threshold. Positive correlation between the difference of the
 57 second and first AP threshold and the first AHP amplitude (computed here relatively to the first pre-AP
 58 potential). Right, faster AHP repolarization produced larger hyperpolarization of AP threshold. Negative
 59 correlation between the difference of the second and first AP threshold and the first AHP slope. **D:** distribution
 60 of the AP threshold relative to V_{rest} (first AP of each burst is excluded), normalized so that 1 (dashed line)
 61 corresponds to the maximum V_m reached during rest. **E:** More negative values of relative AP thresholds were
 62 associated with bursts having higher number of APs (left) and higher intra-burst frequencies (right). Results in
 63 panels C and E are presented as in Figure 3C. **See Extended Data (extended data figure 6-1, and 6-2) for**
 64 **statistic details and individual-cell fit results. The relationship between AHP characteristics and firing**
 65 **properties can be found in extended data figure 6-3. Examples of the characteristics of evoked firing can be**
 66 **found in extended data figure 6-4.**
 67

68 **Fig 7: Influence of resting potential on burst size and frequency.** **A-B:** Linear fits between burst firing
 69 properties and resting potential preceding the burst (V_{rest}); results being presented as in Figure 3C. (A) Burst
 70 size (number of APs) increased with V_m depolarization (B), Intra-burst frequency increased with V_m
 71 depolarization. **Statistics details and single cell fit results are shown in Extended Data (extended data figure**
 72 **7-1 A and B).**
 73

74 **Fig 8: Bursts are terminated by the onset of a slow AHP component.** **A:** Left, evolution along the burst of the
 75 normalized AP threshold (linear interpolation between 0 and 1 which were the resting potential and the
 76 maximum amplitude of subthreshold fluctuations respectively). To compare between bursts, data were shifted
 77 and aligned at 0 for the second AP threshold. We observed a clear but small increase of normalized AP
 78 threshold during burst. Right, histograms of normalized AP thresholds for the second AP (blue) and last AP
 79 (green) in bursts (left panel). Percentiles give the proportion of data above 1. **B:** Examples of bursts with
 80 detected AP threshold (red dots) and their model fits (green cross). Dashed red lines set the predicted threshold
 81 as function of time elapsed after the beginning of the last AHP. We noted that bursts could be either followed by
 82 post-burst rebound (right) or not (left). In both cases the V_m stayed below the predicted AP threshold,
 83 accounting for the end of the burst, and a sudden decay of V_m repolarization rate was observed. See text and
 84 methods for the model details. **C:** As shown in B, we could detect when the V_m goes above the predicted
 85 threshold (overshoot) without producing a further AP. Left pie chart shows the proportion of bursts with a
 86 predicted overshoot (pooled across cells). Middle, pie chart shows the proportion of cells with at least one
 87 predicted overshoot among their bursts. Right, distribution of the differences between predicted AP threshold
 88 (at the same ISI as the last burst ISI) and the threshold of the last AP in the burst **D:** Median traces of the 500
 89 ms following the last AHP peak with exponential fits of the slow AHP component (computed from 50 ms to 500
 90 ms following AHP peak). Upper and lower panels correspond to cells shown in B left and right, respectively. **E:**
 91 Distribution of the time constant of the exponential fits shown in D for all 42 cells (see methods for details). **The**
 92 **evolution of the AHP characteristics along the burst can be found in Extended Data (extended data figure 8-**
 93 **1).**

94

95 **Fig 9: The AHP evolution with the number of APs was mainly due to 4AP sensitive component. A:**
96 *Superposition of the last AHP of evoked trains comprising different number of APs. Stars indicate the onset of*
97 *the slow AHP component i.e. at which the “Vm at slow AHP” was measured. B:* Same neuron as A but in
98 *presence of 4AP (3 mM). C: Modification of AHP, as a function of the number of APs in the trains, in control*
99 *condition and in presence of 4AP. D: Modification of AHP area, as a function of the number of APs in the*
00 *trains, in control condition and in presence of 4AP. E: Modification of the Vm at which the slow component*
01 *appeared, as a function of the number of APs in the bursts, in control condition and in presence of 4AP. F:*
02 *Neuron model showing the superposition of the last AHP at the end of evoked trains comprising different*
03 *numbers of APs. Top Left, with only Nav and Kdr channels in the model, there was no evolution of the AHP with*
04 *the number of APs. Top Middle and Right. Adding I_A current in the model reproduced the evolution of the slow*
05 *AHP observed in experimental data. Bottom; evolution of I_A current during the AHP. I_A , channels biophysics*
06 *from (Rubin and Cleland, 2006); I_A modified, channels biophysics closer to Amendola and colleagues (2012).*
07 *Error bars represent 95% Confidence Interval. N = 11 MCs.*

08

09 **Fig 10: Model of the intrinsic mechanisms accounting for MC firing. A:** Transitions of Nav channel between
10 *deinactivated and inactivated make the AP threshold dependent on Vm fluctuations. Due to the delayed*
11 *deinactivation/inactivation kinetics the threshold fluctuation (red dashed line) is slightly shifted compared to*
12 *Vm fluctuations (blue line). The generation of the AP is favored by excitatory inputs occurring just after the*
13 *negative phase of Vm fluctuations or, when the repolarization phase of inhibitory inputs is rapid enough to*
14 *overcome the shifted threshold before the latter goes back to the pre-AP values. B:* The fast AHP brings the AP
15 *threshold below the V_{rest} and its repolarization rate is rapid enough to overcome the modified threshold, acting*
16 *in this way as a regenerative mechanism that sustains the burst. The slow components of the AHP develop*
17 *gradually along the successive APs. When the Vm at which the slow component should appear is above the shift*
18 *of AP threshold, the manifestation of the slow component is bypassed by the AP generation. Indeed, the slow*
19 *AHP can manifest itself only at Vm more negative than the AP threshold shift. When this happens, the Vm*
20 *repolarization during the slow component is not fast enough to overcome the AP threshold, which then returns*
21 *to the pre-burst value, and the burst stops. For a stronger shift, the AP threshold is reached earlier, during the*
22 *repolarization phase of the fast AHP, and the intraburst frequency is higher. For stronger shift of AP threshold,*
23 *a higher number of APs is necessary so that the slow AHP could manifest itself and thus, the burst duration*
24 *increases. C: The threshold shift is larger when the fast AHP is larger and faster. In such conditions, the bursts*
25 *are longer and have higher intra-burst frequency. D: The AP threshold shift is larger when the V_{rest} of the MC*
26 *is more depolarized, because of modifications of AHP properties and partial inactivation of Nav channels. As a*
27 *consequence, Vm depolarization makes bursts longer and with higher intra-burst frequency*

28

29

30

31

32 **Extended data legends**

33

34 **Extended data Fig 5-1** : Modification of MC AP-threshold and hyperpolarization effects over time and after
35 applications of Na⁺ and Ca²⁺ channels antagonists. **A**) Timing of experiments during which AP threshold was
36 measured after 5 and 10 min, in control conditions or after different pharmacological applications. **B**) AP
37 threshold was significantly increased by blockade of Na⁺ channels with TTX, but not by the antagonist of T-
38 types Ca²⁺ channels (ML218: 5-10 μM). Note the spontaneous increase of threshold with time in control
39 condition, both at 5min and 10 min, with a small difference, possibly due to cell dialysis. The statistical analysis
40 compared to Ctrl0 is depicted above the data points. Values are expressed as modification of AP threshold
41 compared to the control condition at time 0. **C, D**) The effect of membrane hyperpolarization on the AP
42 threshold was stable with time. **E**) The antagonist of T-type channels, ML218, did not affect the modification of
43 AP threshold produced by membrane hyperpolarization. ES = effect size. Horizontal and vertical bars represent
44 95% Confidence Interval

45

46 **Extended Data Figure 6-1:**

47 Characteristics of the first AHP determined the negative shift of AP threshold between the first AP and
48 second AP of the burst. **A**: Distributions of slopes and correlation coefficients of the linear correlations
49 performed in Fig. 6C left of the main manuscript (slope: 0.35 ± 0.10 mV/mV, ES=1.03, R: 0.42 ± 0.09 , T-
50 test $t = 9.34$, $p < 0.0001$, N=49). Darker dots correspond to individual fits with $p < 0.05$ (Pearson
51 correlation, corrected for multiple comparisons). **B**: Distributions of slopes and correlation coefficients
52 of the linear correlations performed in Fig. 6C right of the main manuscript (slope: -5.6 ± 1.5
53 mV/(mV/ms), ES=-1.04, R: -0.47 ± 0.09 , T-test $t = -10.4$, $p < 0.0001$, N=49). Darker dots correspond to
54 individual fits with $p < 0.05$ (Pearson correlation, corrected for multiple comparisons). **C**: Linear
55 correlation between average first AHP amplitude and average negative shift of AP threshold (slope: 0.33
56 mV/mV, R=0.57, Wald test: $p < 0.001$, N=49). Each dot represents the average values for a given cell. **D**:
57 Linear correlation between average first AHP slope and average negative shift of AP threshold (slope: $-$
58 3.4 mV/(mV/ms), R=-0.7, Wald test: $p < 0.001$, N=49). Each dot represents the average values for a given
59 cell.

60

61 **Extended Data Figure 6-2 :**

62 Influence of intra-burst relative AP threshold on burst size (number of APs) and intra-burst AP frequency. **A**:
63 Same analysis as in Figure 6D of the main manuscript but for each MC. **B1**: Distributions of slopes and
64 correlation coefficients of the linear correlations performed in Fig. 6E left of the main manuscript (slope: -4.87
65 ± 2.22 AP/mV, ES = -0.62, R: -0.37 ± 0.08 , T- test $t = -9.56$, $p < 0.0001$, N =49). Darker dots correspond

66 to individual fits with $p < 0.05$ (Pearson correlation, corrected for multiple comparisons). **B2:**
 67 Distributions of slopes and correlation coefficients of the linear correlations performed in Fig. 6E right of the
 68 main manuscript (slope: -4.46 ± 1.00 Hz/mV, ES = -1.26, R: -0.59 ± 0.10 , T-test $t = -11.9$, $p < 0.0001$, $N = 49$).
 69 Correlation between the intra-burst frequency and relative AP threshold: individual-cell fit results from data
 70 shown in Fig 5C right: average slope = -4.46 ± 1.00 Hz/mV, ES = -1.26, average R = -0.59 ± 0.10 , T-test $t = -$
 71 11.9 , $p < 0.0001$, $N = 49$ Darker dots correspond to individual fits with $p < 0.05$ (Pearson correlation,
 72 corrected for multiple comparisons). **C1:** Linear correlation between average relative AP threshold and
 73 average burst size (R: correlation coefficient, p: Wald test p-value, $N = 49$). Each dot represents the average
 74 values for a given cell. **C2:** Linear correlation between average relative AP threshold and average intra-burst
 75 frequency (R: correlation coefficient, p: Wald test p-value, $N = 49$). Each dot represents the average values for
 76 a given cell.

77
 78

79 **Extended Data Figure 6-3:**

80 AHP characteristics determined the firing properties of bursts, namely the burst size and intra-burst AP
 81 frequency.

82

83 **A:** Larger AHP amplitudes were associated with longer bursts. **A1:** Left, Correlations between AHP
 84 amplitude and burst size are found in a cell per cell analysis. Right, Distributions of slopes and correlation
 85 coefficients (slope: -2.98 ± 1.92 AP/mV, ES = -0.43, R : -0.13 ± 0.12 , T-test $t = -2.26$, $p = 0.03$, $N =$
 86 49).

87 Darker dots correspond to individual fits with $p < 0.05$ (Pearson correlation, corrected for multiple
 88 comparisons). **A2:** Linear correlation between average AHP amplitude and average burst size (R:
 89 correlation coefficient, p: Wald test p-value, $N = 49$). Each dot represents the average values for a given
 90 cell. **B:** Larger AHP amplitudes were associated with higher intra-burst frequency. **B1:** Left, Correlations
 91 between AHP amplitude and intra-burst frequency is found in a cell per cell analysis. Right, Distributions of
 92 slopes and correlation coefficients (slope: -3.31 ± 1.36 Hz/mV, ES = -0.69, R: -0.33 ± 0.12 , T-test $t = -5.23$,
 93 $p < 0.0001$, $N = 49$). Darker dots correspond to individual fits with $p < 0.05$ (Pearson correlation, corrected
 94 for multiple comparisons). **B2:** Linear correlation between average AHP amplitude and average intra-burst
 95 frequency (R: correlation coefficient, p: Wald test p-value, $N = 49$). Each dot represents the average values
 96 for a given cell. **C:** Faster AHP repolarizations (i.e. larger AHP slopes) were associated with longer bursts.

97 **C1:** Left, Correlations between AHP slope and burst size are found in a cell per cell analysis. Right,
 98 Distributions of slopes and correlation coefficients (slope: 38.3 ± 22.7 AP/(mV/ms), ES = 0.48, $p = 0.002$;
 99 R

100 = 0.24 ± 0.08 , T-test $t = 5.79$, $p < 0.0001$, $N = 49$). Darker dots correspond to individual fits with $p < 0.05$
 101 (Pearson correlation, corrected for multiple comparisons). **C2:** Linear correlation between average AHP
 102 slope average and burst size (R: correlation coefficient, p: Wald test p-value, $N = 49$). **D:** Faster AHP

03 repolarizations (i.e, larger AHP slopes) were associated with higher intra-burst frequency. **D1:** Left,
 04 Correlations between AHP slope and intra-burst frequency are found in a cell per cell analysis. Right,
 05 Distributions of slopes and correlation coefficients (slope: 71.0 ± 9.0 Hz/(mV/ms), ES = 2.24; R: 0.76
 06 ± 0.07 , T- test $t = 21.7$, $p < 0.0001$, $N = 49$). Darker dots correspond to individual fits with $p < 0.05$
 07 (Pearson correlation, corrected for multiple comparisons). **D2:** Linear correlation between average AHP
 08 slope and average intra-burst frequency (R: correlation coefficient, p: Wald test p-value, $N = 49$). Note that
 09 correlation coefficients were higher when the AHP slope was considered with respect to the AHP amplitude.

11 **Extended data Fig 6-4:**

12
 13 Synaptically evoked bursts are similar to spontaneous bursts. Examples of a cell which displayed a clear
 14 threshold shift between the first two APs (upper panels) and another which did not (lower panels). For each
 15 cell, left panels illustrate side by side a burst evoked by olfactory nerve stimulation and a spontaneous burst.
 16 Black lines show an example of stimulation which failed to evoke a burst. Red dots represent AP thresholds.
 17 Right tables compare features of evoked and spontaneous bursts (for upper cell: 3 evoked and 21 spontaneous
 18 bursts; for lower cell: 5 evoked and 367 spontaneous bursts). Table values are displayed as “mean (SD)”.

20 **Extended Data Figure 7-1:**

21
 22 Influence of resting potential on burst size and intra-burst frequency was linked to the modification of
 23 AP threshold, through changes in AHP characteristics and sodium channels inactivation rates. **A-E:**
 24 Linear fits, slopes and coefficients of the correlations between resting potential beforeburst and burst
 25 firing properties, AP threshold characteristics or AHP characteristics. The first AP threshold in the
 26 burst is not taken into account. The results are presented as in Figure 3C (values are averaged per
 27 burst and fits are done within each cell) **A:** Burst size increased with Vm depolarization. slope: $3.95 \pm$
 28 4.01 AP/mV, ES = 0.28, R: 0.32 ± 0.10 , T-test $t = 6.06$, $p < 0.0001$, $N = 49$ (left panel: identical to Fig
 29 7A). **B:** Intra-burst frequency increased with Vm depolarization. slope: 2.90 ± 2.41 Hz/mV, ES = 0.34,
 30 R: 0.37 ± 0.13 , T-test $t = 5.49$, $p < 0.0001$, $N = 49$ (left panel: identical to Fig 7B). **C:** Relative AP
 31 threshold became more negative with Vm depolarization. slope: -0.97 ± 0.29 mV/mV, ES = -0.94, R: -
 32 0.64 ± 0.10 , T-test $t = -12.3$, $p < 0.0001$, $N = 49$. **D:** AHP amplitude increased with Vm
 33 depolarization. slope: -0.59 ± 0.55 Hz/mV, ES = -0.30, R: -0.51 ± 0.14 , T-test $t = -7.32$, $p < 0.0001$, N
 34 $= 49$. **E:** AHP repolarization speed increased with Vm depolarization. slope: 0.036 ± 0.014
 35 (mV/ms)/mV, ES = 0.73, average R: 0.33 ± 0.11 , T-test $t = 5.75$, $p < 0.0001$, $N = 49$. **F:** Cells with a
 36 more depolarized Vrest showed a greater effect of pre-AP potential on AP threshold. In this panel all
 37 the spikes of the burst are analyzed. For the first spike, pre-AP potential is the most hyperpolarized
 38 value of membrane potential preceding the burst while for the other APs, it corresponds to the
 39 negative peak of the preceding AHP (see Fig 1). Note that slopes of the correlation between relative

40 AP threshold and pre-AP potential were bigger at more depolarized V_{rest} (i.e, the effect of a given
41 hyperpolarization on AP threshold is bigger when resting potential is more depolarized). **G:**
42 Simulation of the effect of V_m hyperpolarization on AP threshold at different resting potential. It
43 shows an amplification of the AP threshold shift produced by membrane hyperpolarization when the
44 resting potential was more depolarized (note the change of the slope of the correlation between AP
45 threshold modification and pre-spike hyperpolarization). **H:** Modification of AP threshold as a
46 function of the quantity of N_{av} conductance available before the spike in the computational model.
47 The dots represent the quantity of available N_{av} conductance at resting potential or after 10 mV of
48 hyperpolarization. Note that the same 10 mV membrane hyperpolarization produced a stronger
49 modification of AP threshold when resting potential was more depolarized.

50
51 **Extended Data Figure 8-1:**

52 Evolution of AHP parameters during bursts. **A:** Same graphs as in Figure 8A (main manuscript) but for AHP
53 amplitude preceding the AP. Left panel: Distributions of AHP amplitude before the second AP and the last AP
54 of the burst. There was a small decrease of AHP amplitude from the 2nd to last spike (0.46 ± 0.04 mV, paired t -
55 test: $t = 23.5$, $p < 0.001$, $N = 1276$, $ES = 0.65$). Right panel shows that there was a small decrease of absolute
56 AHP amplitude from 2nd to 3rd AP in burst, but after 3rd AP in burst the average AHP amplitude was constant.
57 **B:** Same graphs as in Figure 8A (main manuscript) but for AHP slope preceding the AP. Left panel:
58 Distributions of AHP slope before the second AP and the last AP of the burst. There was a decrease of AHP
59 slope from 2nd to last AP (-132 ± 9 mV/ms, paired t -test: $t = -27.8$, $p < 0.001$, $N = 1276$, $ES = -0.77$). Right
60 panel shows that the decrease of AHP slope occurs mainly during the firsts 10 APs in burst

964

965

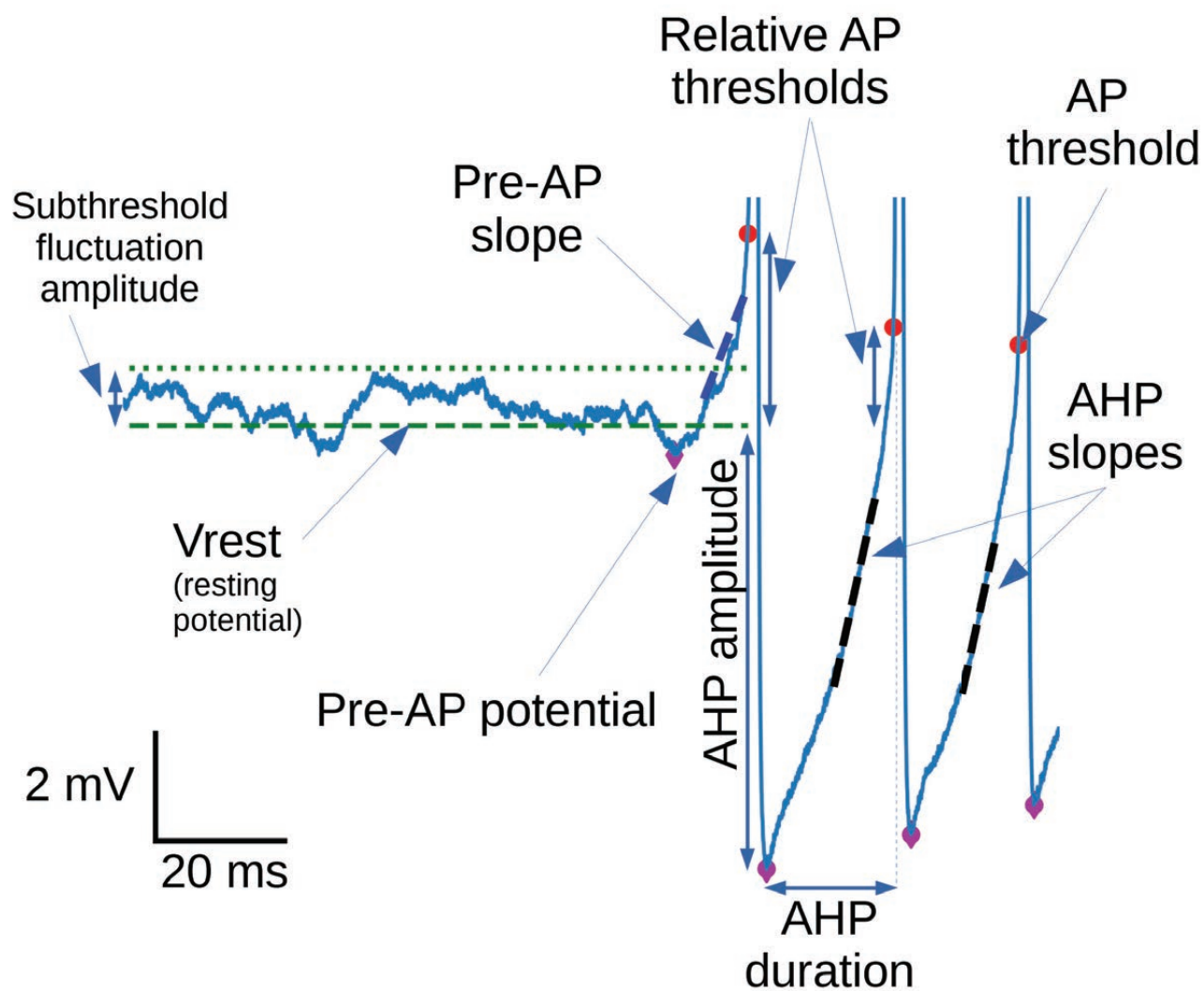
966

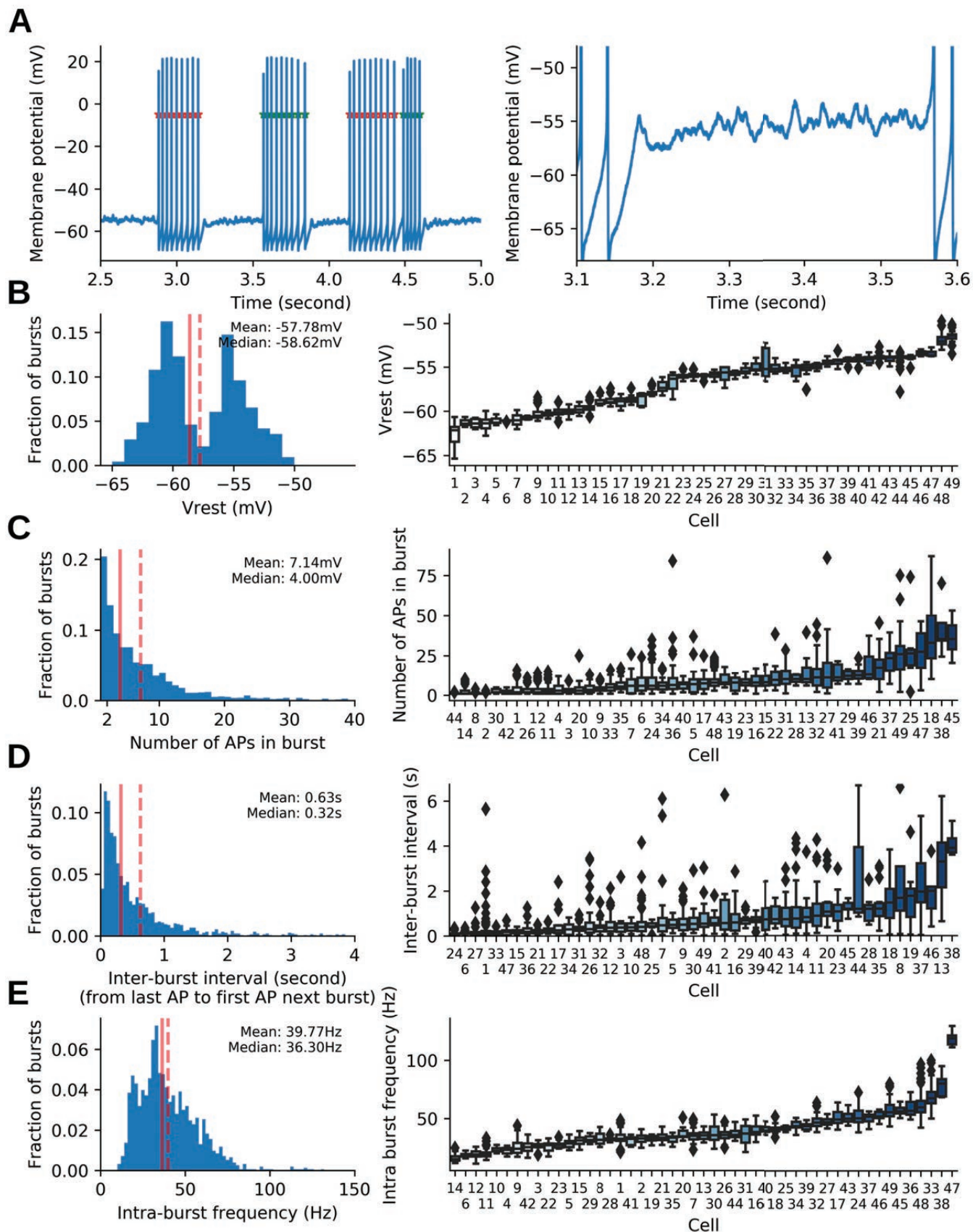
967 **References:**

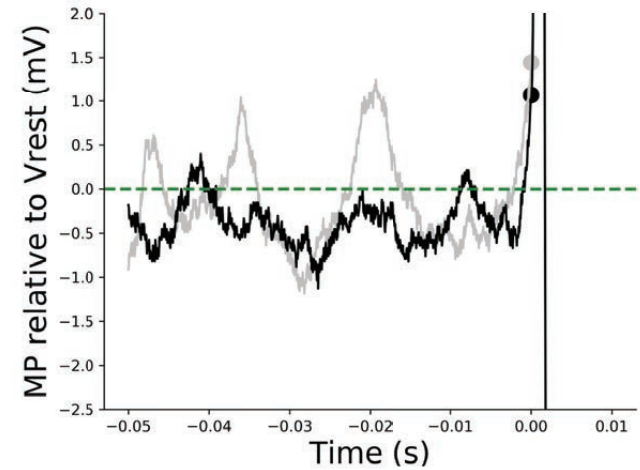
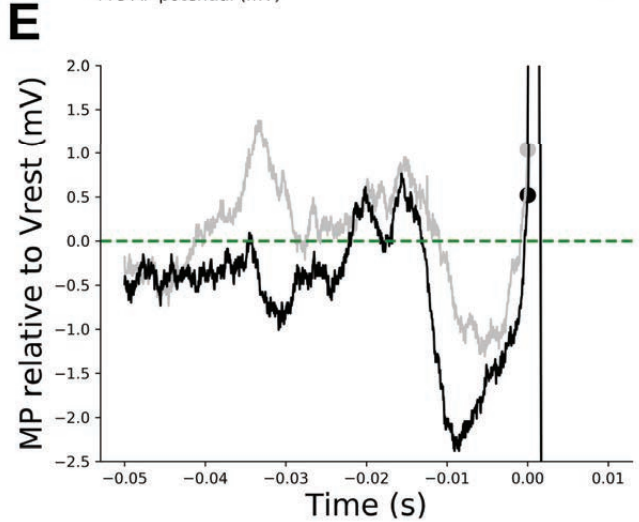
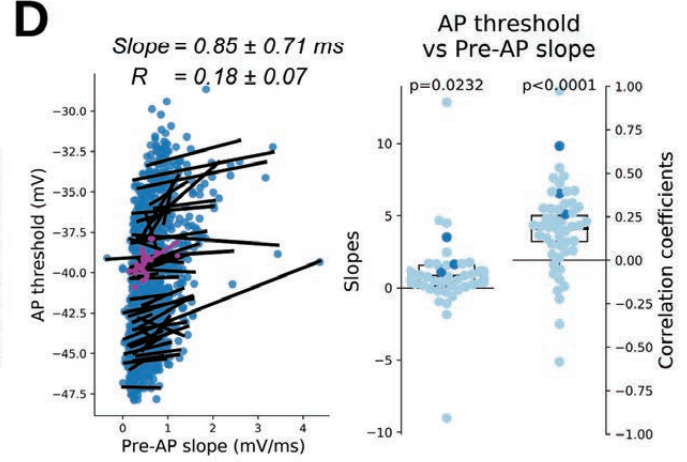
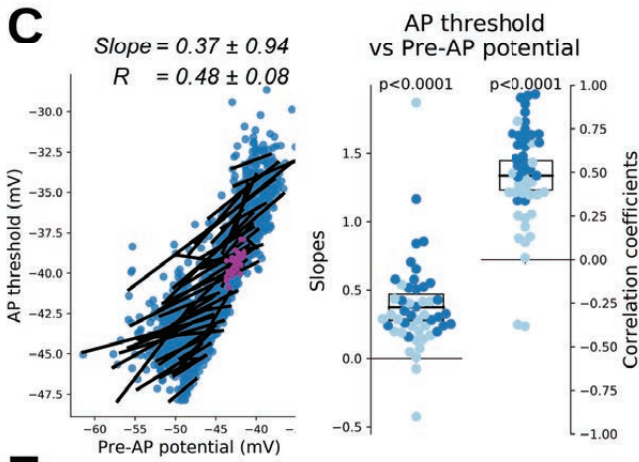
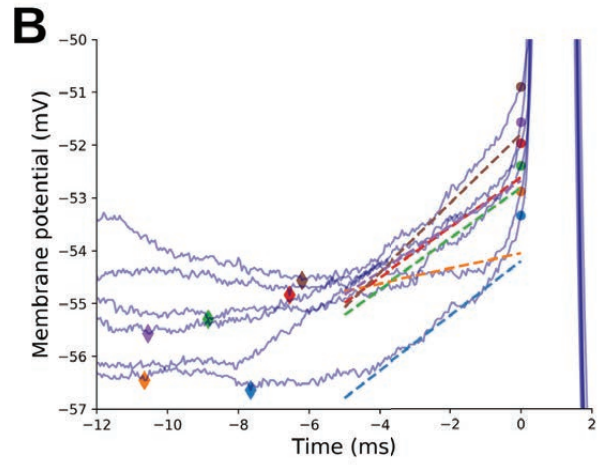
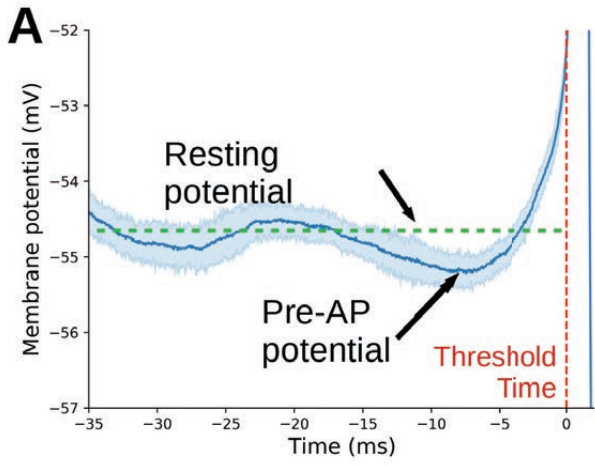
- 968 Adelman JP, Maylie J & Sah P (2012). Small-conductance Ca²⁺-activated K⁺ channels: form
969 and function. *Annu Rev Physiol* **74**, 245–269.
- 970 Amendola J, Woodhouse A, Martin-Eauclaire M-F & Goillard J-M (2012). Ca²⁺/cAMP-
971 sensitive covariation of I(A) and I(H) voltage dependences tunes rebound firing in
972 dopaminergic neurons. *J Neurosci* **32**, 2166–2181.
- 973 Andrade R, Foehring RC & Tzingounis AV (2012). The calcium-activated slow AHP: cutting
974 through the Gordian knot. *Front Cell Neurosci* **6**, 47.
- 975 Aroniadou-Anderjaska V, Ennis M & Shipley MT (1999). Dendrodendritic recurrent excitation
976 in mitral cells of the rat olfactory bulb. *J Neurophysiol* **82**, 489–494.
- 977 Azouz R & Gray CM (2003). Adaptive coincidence detection and dynamic gain control in
978 visual cortical neurons in vivo. *Neuron* **37**, 513–523.
- 979 Balu R, Larimer P & Strowbridge BW (2004). Phasic stimuli evoke precisely timed spikes in
980 intermittently discharging mitral cells. *J Neurophysiol* **92**, 743–753.
- 981 Balu R & Strowbridge BW (2007). Opposing Inward and Outward Conductances Regulate
982 Rebound Discharges in Olfactory Mitral Cells. *Journal of Neurophysiology* **97**, 1959–
983 1968.
- 984 Brosh I, Rosenblum K & Barkai E (2006). Learning-induced reversal of the effect of
985 noradrenalin on the postburst AHP. *J Neurophysiol* **96**, 1728–1733.
- 986 Burton SD & Urban NN (2014). Greater excitability and firing irregularity of tufted cells
987 underlies distinct afferent-evoked activity of olfactory bulb mitral and tufted cells. *J*
988 *Physiol* **592**, 2097–2118.
- 989 Cain SM & Snutch TP (2010). Contributions of T-type calcium channel isoforms to neuronal
990 firing. *Channels (Austin)* **4**, 475–482.
- 991 Chen WR & Shepherd GM (1997). Membrane and synaptic properties of mitral cells in slices
992 of rat olfactory bulb. *Brain Res* **745**, 189–196.
- 993 Deister CA, Chan CS, Surmeier DJ & Wilson CJ (2009). Calcium-activated SK channels
994 influence voltage-gated ion channels to determine the precision of firing in globus
995 pallidus neurons. *J Neurosci* **29**, 8452–8461.
- 996 Desmaisons D, Vincent JD & Lledo PM (1999). Control of action potential timing by intrinsic
997 subthreshold oscillations in olfactory bulb output neurons. *J Neurosci* **19**, 10727–
998 10737.

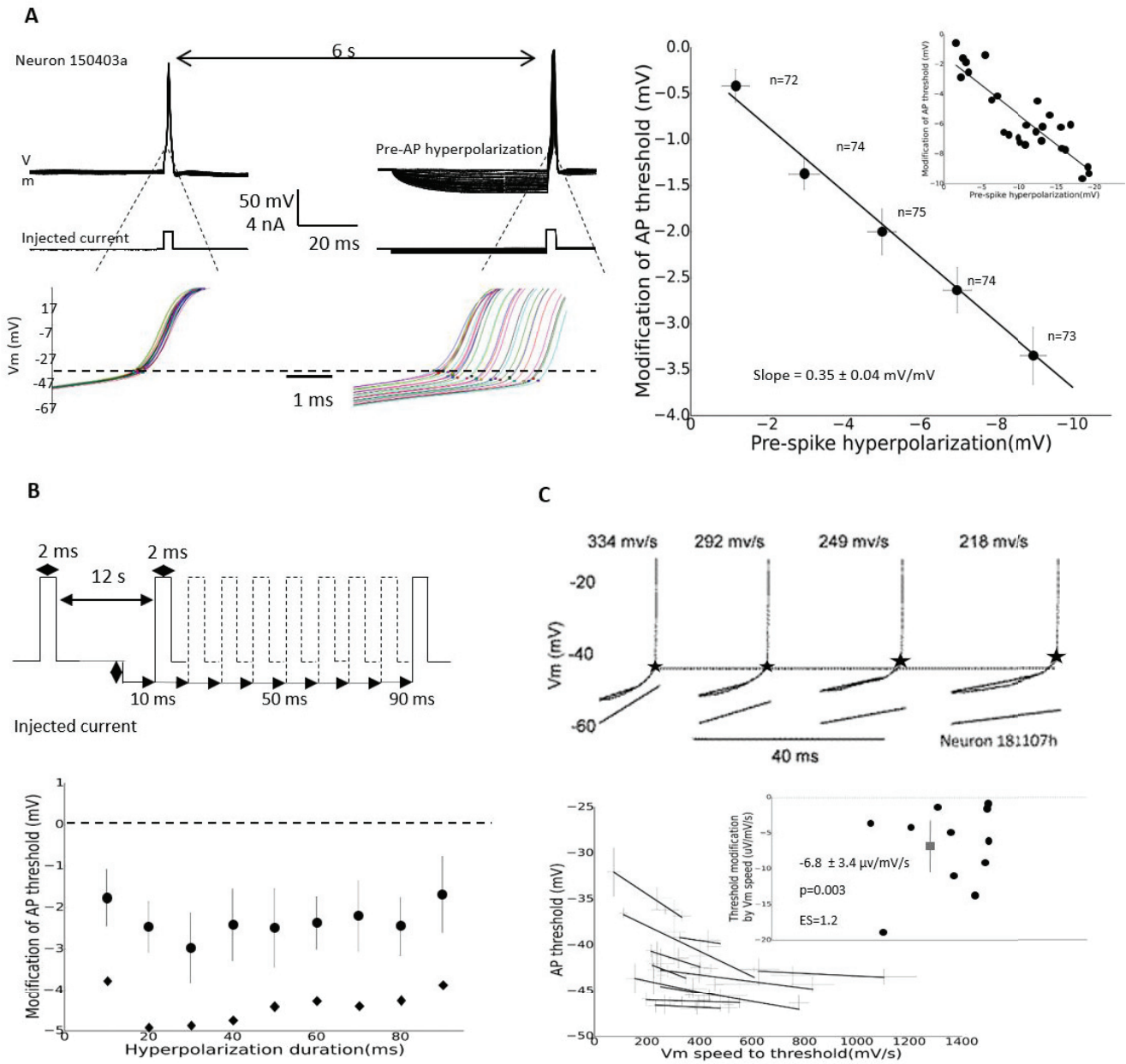
- 999 Duméniéu M, Fourcaud-Trocmé N, Garcia S & Kuczewski N (2015). Afterhyperpolarization
1000 (AHP) regulates the frequency and timing of action potentials in the mitral cells of the
1001 olfactory bulb: role of olfactory experience. *Physiol Rep*; DOI: 10.14814/phy2.12344.
- 1002 Faber ESL & Sah P (2007). Functions of SK channels in central neurons. *Clin Exp Pharmacol*
1003 *Physiol* **34**, 1077–1083.
- 1004 Friedman D & Strowbridge BW (2000). Functional role of NMDA autoreceptors in olfactory
1005 mitral cells. *J Neurophysiol* **84**, 39–50.
- 1006 Henze DA & Buzsáki G (2001). Action potential threshold of hippocampal pyramidal cells in
1007 vivo is increased by recent spiking activity. *Neuroscience* **105**, 121–130.
- 1008 Hu W, Tian C, Li T, Yang M, Hou H & Shu Y (2009). Distinct contributions of Na(v)1.6 and
1009 Na(v)1.2 in action potential initiation and backpropagation. *Nat Neurosci* **12**, 996–
1010 1002.
- 1011 Isaacson JS & Strowbridge BW (1998). Olfactory reciprocal synapses: dendritic signaling in
1012 the CNS. *Neuron* **20**, 749–761.
- 1013 Iyer R, Ungless MA & Faisal AA (2017). Calcium-activated SK channels control firing regularity
1014 by modulating sodium channel availability in midbrain dopamine neurons. *Sci Rep* **7**,
1015 5248.
- 1016 Kollo M, Schmaltz A, Abdelhamid M, Fukunaga I & Schaefer AT (2014). “Silent” mitral cells
1017 dominate odor responses in the olfactory bulb of awake mice. *Nat Neurosci* **17**,
1018 1313–1315.
- 1019 Leng G, Hashimoto H, Tsuji C, Sabatier N & Ludwig M (2014). Discharge patterning in rat
1020 olfactory bulb mitral cells in vivo. *Physiol Rep* **2**, e12021.
- 1021 Li T, Tian C, Scalmani P, Frassoni C, Mantegazza M, Wang Y, Yang M, Wu S & Shu Y (2014).
1022 Action potential initiation in neocortical inhibitory interneurons. *PLoS Biol* **12**,
1023 e1001944.
- 1024 Padmanabhan K & Urban NN (2010). Intrinsic biophysical diversity decorrelates neuronal
1025 firing while increasing information content. *Nat Neurosci* **13**, 1276–1282.
- 1026 Platkiewicz J & Brette R (2011). Impact of fast sodium channel inactivation on spike
1027 threshold dynamics and synaptic integration. *PLoS Comput Biol* **7**, e1001129.
- 1028 Reuveni I & Barkai E (2018). Tune it in: mechanisms and computational significance of
1029 neuron-autonomous plasticity. *J Neurophysiol* **120**, 1781–1795.
- 1030 Rinberg D, Koulakov A & Gelperin A (2006). Sparse odor coding in awake behaving mice. *J*
1031 *Neurosci* **26**, 8857–8865.
- 1032 Rubin DB & Cleland TA (2006). Dynamical mechanisms of odor processing in olfactory bulb
1033 mitral cells. *J Neurophysiol* **96**, 555–568.
- 1034 Sah P & Faber ESL (2002). Channels underlying neuronal calcium-activated potassium
1035 currents. *Prog Neurobiol* **66**, 345–353.

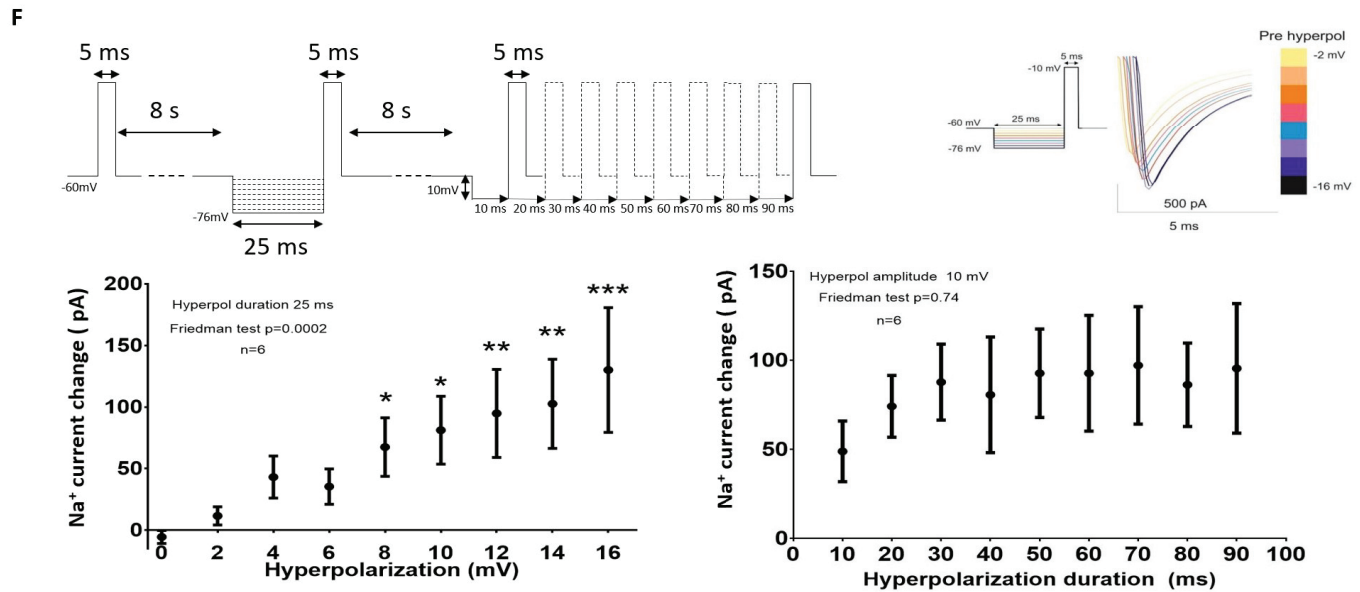
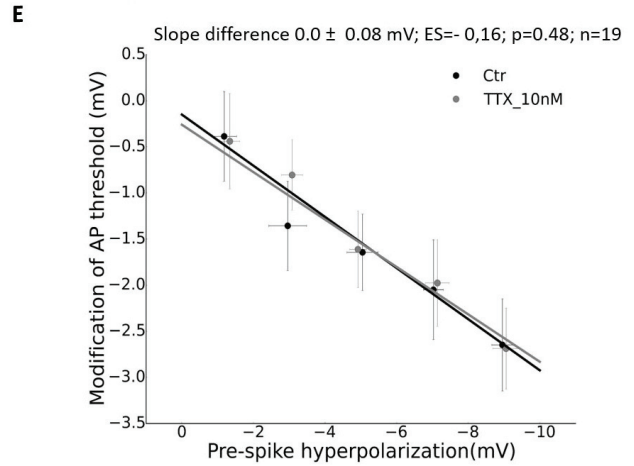
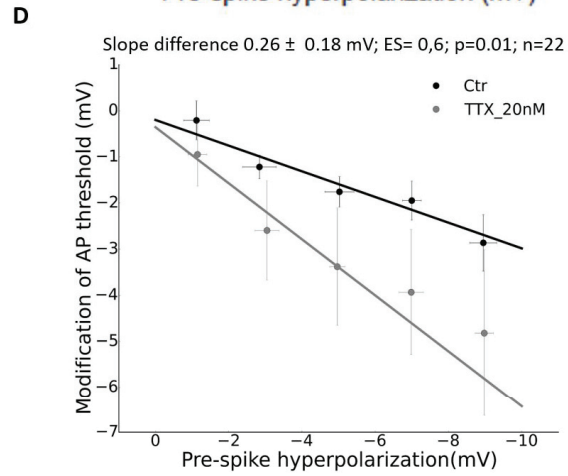
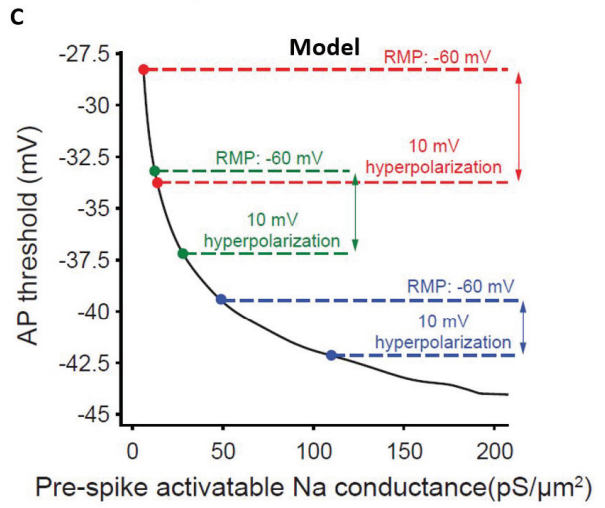
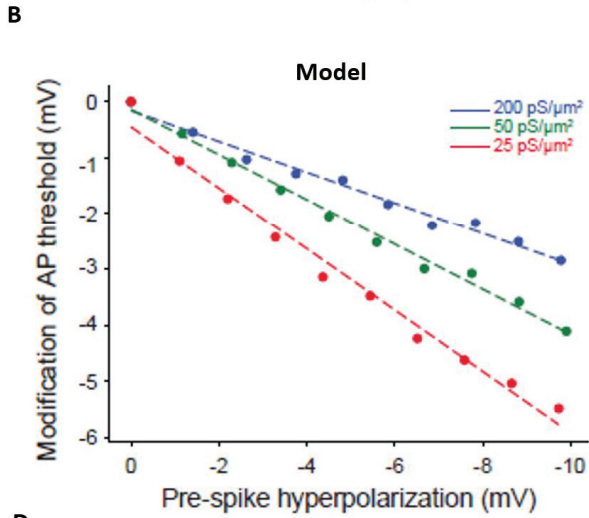
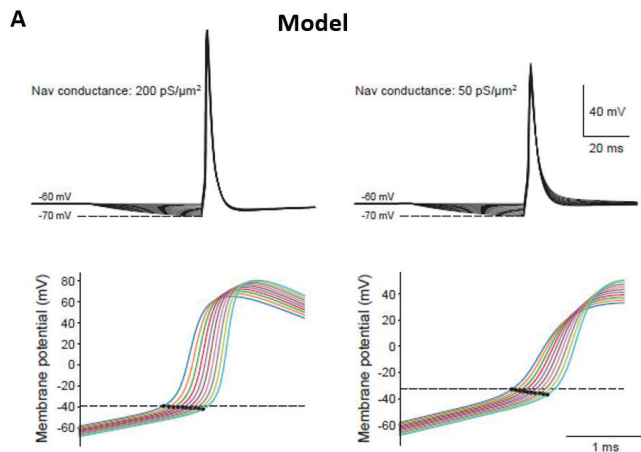
- 1036 Salin PA, Lledo PM, Vincent JD & Charpak S (2001). Dendritic glutamate autoreceptors
1037 modulate signal processing in rat mitral cells. *J Neurophysiol* **85**, 1275–1282.
- 1038 Schoppa NE, Kinzie JM, Sahara Y, Segerson TP & Westbrook GL (1998). Dendrodendritic
1039 inhibition in the olfactory bulb is driven by NMDA receptors. *J Neurosci* **18**, 6790–
1040 6802.
- 1041 Schwindt PC, Spain WJ, Foehring RC, Stafstrom CE, Chubb MC & Crill WE (1988). Multiple
1042 potassium conductances and their functions in neurons from cat sensorimotor cortex
1043 in vitro. *J Neurophysiol* **59**, 424–449.
- 1044 Tripathy SJ, Padmanabhan K, Gerkin RC & Urban NN (2013). Intermediate intrinsic diversity
1045 enhances neural population coding. *Proc Natl Acad Sci USA* **110**, 8248–8253.
- 1046 Wu WW, Oh MM & Disterhoft JF (2002). Age-related biophysical alterations of hippocampal
1047 pyramidal neurons: implications for learning and memory. *Ageing Res Rev* **1**, 181–
1048 207.
- 1049 Yu Y, Burton SD, Tripathy SJ & Urban NN (2015). Postnatal development attunes olfactory
1050 bulb mitral cells to high-frequency signaling. *J Neurophysiol* **114**, 2830–2842.
- 1051 Zhou P, Burton S, Urban N & Ermentrout GB (2013). Impact of neuronal heterogeneity on
1052 correlated colored noise-induced synchronization. *Front Comput Neurosci*; DOI:
1053 10.3389/fncom.2013.00113.
- 1054
- 1055
- 1056
- 1057

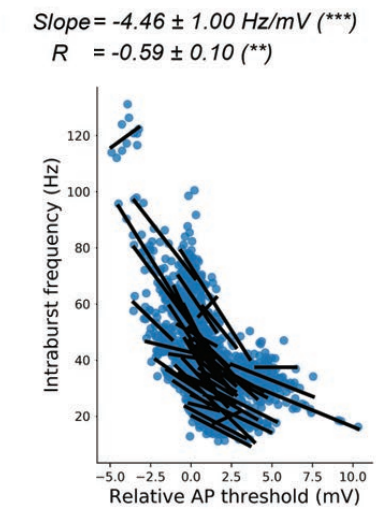
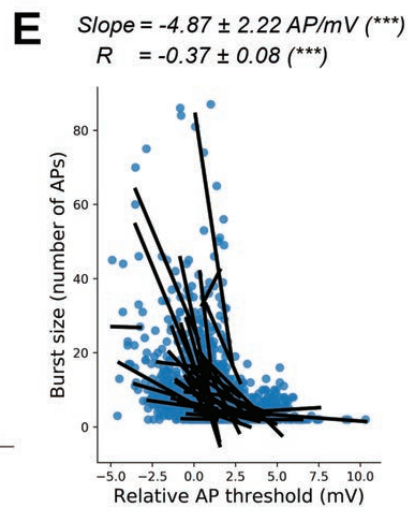
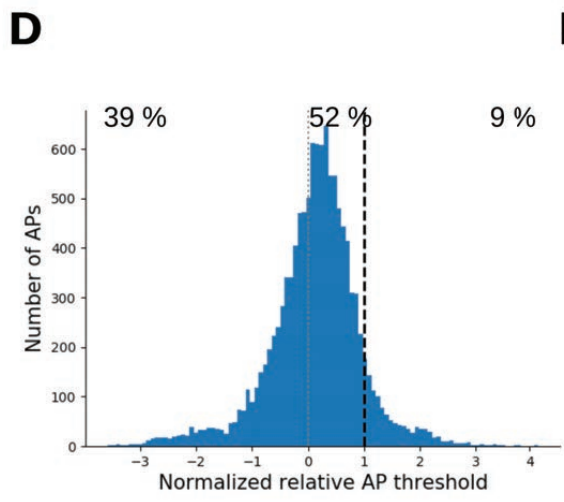
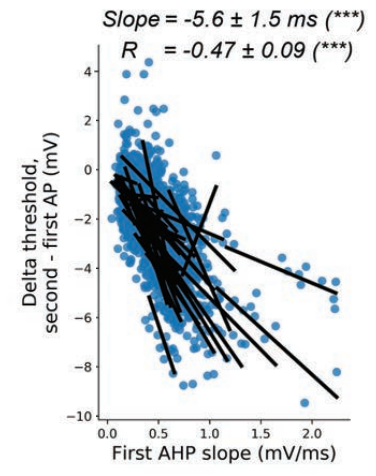
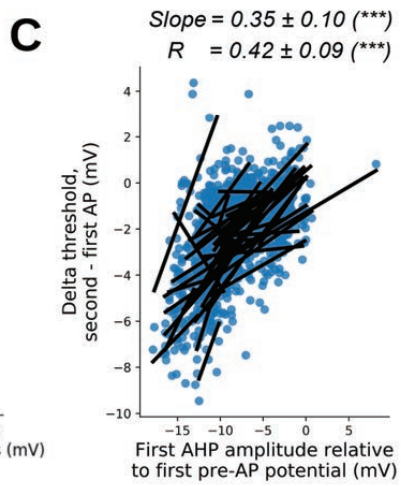
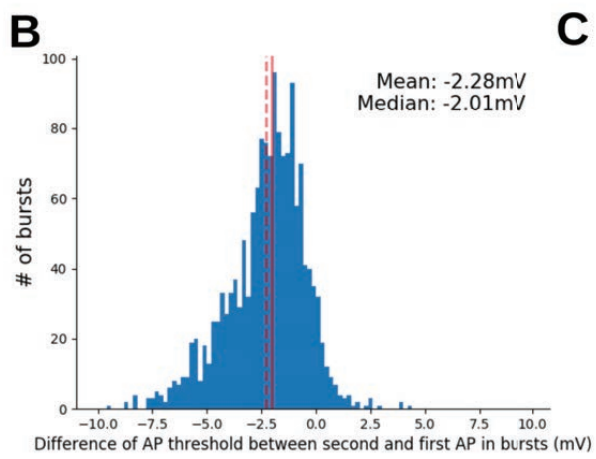
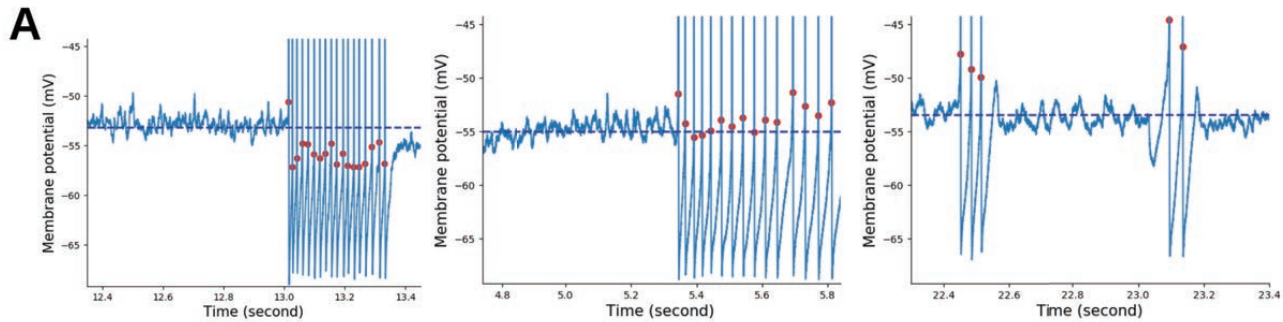




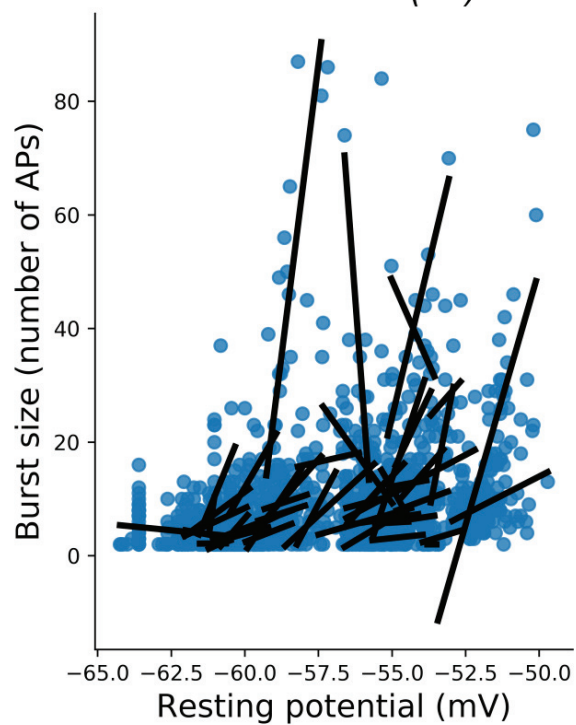








A Slope = 3.95 ± 4.01 AP/mV (n.s.)
 $R = 0.32 \pm 0.10$ (***)



B Slope = 2.90 ± 2.41 Hz/mV (*)
 $R = 0.37 \pm 0.13$ (***)

